Classification of IMAGE/RPI-stimulated plasma resonances for the accurate determination of magnetospheric electron-density and magnetic-field values

R. F. Benson[1], V. A. Osherovich[2], J. Fainberg[1], B. W. Reinisch[3]

[1]NASA/Goddard Space Flight Center, Greenbelt, Maryland
[2]L-3 Analytics/Goddard Space Flight Center, Greenbelt, Maryland
[3]Center for Atmospheric Research, University of Massachusetts Lowell, Lowell, Massachusetts.

Abstract. The Radio Plasma Imager (RPI) on the Imager for Magnetopause-to-Aurora Global Exploration (IMAGE) satellite stimulates short-range plasma-wave echoes and plasma emissions, both known as local plasma resonances, that are detected on plasmagrams (virtual range vs. frequency presentations of the amplitude-modulated received signals). These resonances are used to provide the local electron density N_e and magnetic field strength $|\mathbf{B}|$ that are required for accurate inversions of the RPI reflection traces into magnetospheric N_e profiles. Examples are presented that have been used for this purpose and also that yield N_e gradients within a single plasmagram in the vicinity of the plasmapause and accurate (near apogee) N_e measurements during the 31 March 2001 magnetic storm. The RPI-stimulated resonances are the magnetospheric analog of plasma resonances stimulated by ionospheric topside sounders at the harmonics of the electron cyclotron frequency f_{ce}, the electron plasma frequency f_{pe}, the upper-hybrid frequency f_{uh} (where $f_{uh}^2 = f_{pe}^2 + f_{ce}^2$), between nf_{ce} both above and below f_{pe} known as Qn and Dn resonances, respectively, and also at other frequencies. While they are observed to have an inherent bandwidth of 300 Hz or less, the effective detection bandwidth for strong resonances is nearly 2 kHz. The Qn resonances are often observed with time durations exceeding the 178 ms limit of the RPI operating programs commonly used for resonance detection. The f_{uh} resonance is also observed with a long time duration even when it is in the plasma domain where it is normally weaker, i.e., when $f_{uh} > 2f_{ce}$. A strong resonance at f_{pe} is often, but not always, observed. In earlier investigations, the Dn resonances had been related to natural magnetospheric plasma-wave emissions and to sounder-stimulated plasma-wave emissions in Jupiter's Io plasma torus. The present RPI observations represent the first evidence for the stimulation of these resonances by a sounder deep in the terrestrial magnetosphere. These observations suggest the possible widespread occurrence of N_e field-aligned irregularities (FAI), or the ease of sounder-stimulated FAI, based on one Dn generation mechanism involving eigen modes of cylindrical plasma oscillations which have been associated with FAI. The RPI observations provide additional support to earlier suggestions that the Qn and Dn resonances have components of natural origin. The capability of simultaneous reception on three mutually orthogonal dipole receiving antennas often aids in the identification of spectral features. The RPI capability to generate magnetospheric reflection traces, leading to well-defined wave cutoff frequencies at the satellite, provides independent Ne determinations and additional spectral-identification confidence. Combining these capabilities with new analysis techniques that produce three-antenna plasmagrams normalized by f_{ce} and amplitude plots based on averages over different range-bin intervals, N_e and $|\mathbf{B}|$ can often be accurately determined from the plasma-resonance

spectra to within uncertainties of the order of 1% and 0.1%, respectively, when RPI sounds using frequency steps equal to the 300 Hz receiver bandwidth. Such accuracy in magnetospheric N_e determination, even when $N_e \sim 1$ cm^{-3}, is difficult to attain by other techniques. It can only be obtained by RPI with proper spectral-identification. For example, identification uncertainties between f_{pe} and f_{uh} can lead to 20% uncertainties in N_e; even larger uncertainties can result when the N_e determinations are based solely on the Qn resonances and f_{ce} when non-Maxwellian electron velocity distributions are present. Except for such frequency deviations of the Qn resonances, the main controlling factor of the plasma-resonance spectra appears to be, as in the ionosphere, the plasma parameter f_{pe}/f_{ce}.

1. Introduction

The Radio Plasma Imager (RPI) on the Imager for Magnetopause-to-Aurora Global Exploration (IMAGE) satellite stimulates short-range electrostatic (es) echoes and long-range electromagnetic (em) echoes. Both appear on the RPI records called plasmagrams which display the amplitude of the received echo and its virtual range (i.e., assuming free-space speed of light propagation) as a function of the sounding frequency (see *Reinisch et al*. [2000] for a description of the instrument and data formats). The plasmagrams are the magnetospheric analog of topside-sounder ionograms [*Benson et al.*, 1998]. The es echoes form an important subset of a class of signal returns known as plasma resonances. They are called resonances because of their spike-like appearance on ionospheric topside ionograms (and magnetospheric plasmagrams). Most of them have been attributed to the reception of sounder-stimulated es waves of low group velocity that are returned to the spacecraft following the short-duration sounder pulse. They are returned due to the extreme sensitivity of the plasma-wave dispersion relations to slight gradients in the ambient electron density N_e and the ambient magnetic field strength $|\mathbf{B}|$ near characteristic frequencies of the plasma. From rocket and satellite-borne ionospheric sounders, they are known to occur at

$$nf_{ce}(\text{kHz}) \approx n\{0.028\ |\mathbf{B}(\text{nT})|\}\ (n = 2, 3, 4, \ldots) \tag{1}$$

$$f_{pe}(\text{kHz}) \approx \{80.6\ N_e(\text{cm}^{-3})\}^{1/2} \tag{2}$$

$$f_{uh} = (f_{pe}^{\,2} + f_{ce}^{\,2})^{1/2} \tag{3}$$

where f_{ce} is the electron cyclotron frequency, f_{pe} is the electron plasma frequency and f_{uh} is the upper hybrid frequency, (see, e.g., reviews by *Muldrew* [1972a] and *Benson* [1977]). A sequence of resonances known as Qn resonances was discovered on topside ionograms at frequencies between the nf_{ce} harmonics and above f_{uh} by *Warren and Hagg* [1968] who showed that they are observed at the frequencies given by the approximate expression

$$f_{Qn} \approx f_{ce}\{n + (0.464/n^2)(f_{pe}^{\,2}/f_{ce}^{\,2})\} \tag{4}$$

based on the es approximation to the dispersion relation with a Maxwellian electron-velocity distribution and derived for f_{Qn}/f_{ce} values close to integers. *Muldrew* [1972b] showed that they are due to sounder-stimulated es Bernstein-mode waves with group velocity $\mathbf{v_g}$ nearly matched to the satellite velocity $\mathbf{v_s}$. A resonance is also observed at f_{ce} (i.e., n = 1 in (1) above) but the propagation conditions responsible for this resonance have not been established [*Muldrew*, 1972a]. The above plasma resonances have also been observed by low-power sounders designed for resonance detection (called relaxation sounders) deep in the magnetosphere [*Etcheto and Bloch*, 1978].

The purpose of this paper is to demonstrate that all of the above plasma resonances are observed by the RPI on IMAGE in the magnetosphere and that additional phenomena are also observed. These additional phenomena are commonly observed by ionospheric topside sounders, see, e.g., *Benson* [1982], but have not been reported to be present in the magnetospheric relaxation sounder data. They are the following: (1) the wave cutoff frequencies for the fast and slow branches of the extraordinary mode (called the R-X and L-Z modes, respectively) given by

$$f_x = (f_{ce}/2)\ \{1 + (1 + 4\ f_{pe}^2/f_{ce}^2)^{1/2}\} \tag{5}$$

$$f_z = (f_{ce}/2)\ \{-1 + (1 + 4\ f_{pe}^2/f_{ce}^2)^{1/2}\} \tag{6}$$

or, assuming fpe and fce do not change significantly during the recording period, $f_z = f_x - f_{ce}$ (see, e.g., *Stix* [1962]; *Goertz and Strangeway* [1995]), (2) a sequence of resonances know as Dn resonances discovered on topside ionograms at frequencies between the nf_{ce} harmonics and below f_{uh} [*Nelms and Lockwood*, 1967; *Oya*, 1970] which have been shown to obey the following equations

$$f_{Dn} = 0.95\ (f_{pe}f_{ce})^{1/2}n^{1/2} \tag{7}$$

$$f_{Dn}^{+} = (f_{Dn}^2 + f_{ce}^2)^{1/2} \tag{8}$$

$$f_{Dn}^{-} = (f_{Dn}^2 - f_{ce}^2)^{1/2} \tag{9}$$

[*Osherovich*, 1987; *Osherovich*, 1989; *Osherovich and Benson*, 1991], and (3) a prominent diffuse resonance signal between f_{pe} and f_{uh} known as f_{DNT} (from the ionospheric notation of f_N and f_T for f_{pe} and f_{uh}, respectively) when $f_{pe}/f_{ce} \approx 1$ [*Benson*, 1982]. The first two of these additional phenomena have also been observed by high-altitude sounders [*Oya et al.*, 1990]. The third occurs in a frequency region where enhanced signals are common both due to aspect-sensitive scattering of Z-mode signals from N_e field-aligned irregularities (FAI) during active sounding experiments (see, e.g., *Lockwood* [1962], *Muldrew* [1969] and *James* [1979]) and to natural radio emissions (see, e.g., *Beghin et al*. [1989], *Benson* [1993], *Kurth et al*. [2001], *Benson et al*. [2002] and references therein).

The significance of this demonstration is that these wave cutoff and resonant phenomena are of fundamental importance to the extraction of geophysical parameters

from the RPI plasmagrams and to the understanding of fundamental plasma emission processes. Since the phenomena described by (1) – (6) correspond to wave propagation that extends well beyond the disturbed region caused by spacecraft-plasma interactions, but is still fairly local to the satellite, a self-consistent identification of these features can yield accurate determinations of ambient plasma parameters. The starting point is to determine f_{ce}, and hence $|\mathbf{B}|$ from (1), from the observed nf_{ce} resonances. This determination can usually be made to within a few tenths per cent when higher-order nf_{ce} resonances are observed. Such accuracy is important on a magnetospheric satellite such as IMAGE that carries no scientific magnetometer since the model field can be in error by tens of per cent during times of extreme magnetic disturbance [*Osherovich et al.*, 2001]. Next, a self-consistent determination of f_{pe} is made, and hence of N_e from (2), from all the resonances and cutoffs, corresponding to (2)-(6), that are present on the plasmagram under investigation. This determination can usually be made to within a few per cent. (Normally, it is difficult to accurately determine the magnetosphere N_e, e.g., see Section 5 of *Benson et al*. [2001b]). These determinations of f_{ce} and f_{pe} have been used to provide the starting points for the inversion process leading to N_e polar-cap and plasmaspheric profiles [*Reinisch et al.*, 2001a; *Nsumei et al.*, 2002], to relate the observed emission peaks in the RPI passive dynamic spectra to the ambient f_{pe} and f_{uh} values [*Benson et al.*, 2002], to determine the high-altitude magnetospheric plasma response to the large 31 March 2001 magnetic storm [*Osherovich et al.*, 2001], and to relate this response to magnetic–cloud parameters upon magnetospheric impact [*Osherovich et al.*, 2001].

Information concerning fundamental plasma emission processes is provided mainly by the Qn and Dn resonances. Observed deviations of the frequencies of the Qn resonances from (4) provide information concerning the electron distribution function [*Etcheto and Bloch*, 1978]. Confirmation of the existence of the Dn resonances in the Earth's magnetosphere, and that they obey the relations (7) – (9), is of particular importance because these equations result from an interpretation of the Dn resonances that claims that they are signatures of a new mode in plasma physics and that they represent eigenmodes where the electric and magnetic forces are approximately in balance [*Osherovich*, 1987]. These equations provide a method of determining N_e and $|\mathbf{B}|$ independent from the phenomena described by (1) – (6). They have been applied to the interpretation of natural magnetospheric emissions [*Benson and Osherovich*, 1992; *Benson et al.*, 2001b] and active planetary magnetospheric relaxation sounding [*Osherovich et al.*, 1993] and have stimulated considerable controversy [*LeSager et al.*, 1998; *Benson et al.*, 2001a; *Canu*, 2001a; *Canu*, 2001b].

It is important to note that all the frequencies defined by (1) – (3) and (5) - (9) from cold-plasma theory depend only on f_{ce} and f_{pe}. A similar dependence is true for the Qn resonances in a Maxwellian distribution as represented by (4). In the case where electron and ion Maxwellian distributions have the same temperature, the calculated Qn frequencies were not sensitive to the electron temperature value selected (see the discussion pertaining to Figure 4 of *Benson et al*. [2001b]). This primary dependence on f_{pe}/ f_{ce} is illustrated in Figure 1 where all frequencies have been normalized by f_{ce}. Our purpose here is to demonstrate how this diagram can be used to help identify the frequency spectrum of RPI-stimulated plasma resonance phenomena. Our emphasis will be on spectral identification, for the purpose of extracting geophysical parameters, rather

than on the physics of the excitation, propagation and reception of the waves responsible for the observed plasma resonances. In Section 2, sample RPI plasmagrams are presented that illustrate (1) the spectra of sounder-stimulated plasma resonances observed under different plasma conditions, (2) the identification of spectral features and the corresponding determinations of $|\mathbf{B}|$ and N_e, (3) the analysis techniques that aid this spectral identification and (4) a comparison of some of the magnetospheric resonances to their ionospheric counterparts. Section 3 expands on this comparison by reviewing some of the key results from earlier ionospheric topside-sounding and magnetospheric relaxation-sounding research most relevant to identifying and interpreting the spectral features observed by RPI and indicating the similarities and differences between the RPI and the earlier observations. This section also illustrates that caution is necessary in the interpretation if N_e determinations to an accuracy of the order of 1% are desired, and indicates fundamental questions concerning the physics of sounder-stimulated magnetospheric resonances yet to be addressed. A summary is presented in Section 4.

2. Observations

IMAGE is in a polar orbit (approximately 1000 km altitude by 8 R_E radial distance) operating in a reverse cartwheel mode with the long (originally 500 m tip-to-tip) X and Y spin-plane dipole antennas in the orbit plane and the shorter (20 m tip-to-tip) Z dipole antenna parallel to the spin axis (spin rate = 0.5 rpm). Due to events of unknown origin on 3 Oct 2000 and 18 Sep 2001, the X and Y antenna elements were shortened to estimated tip-to-tip lengths of 370 and 470 m, respectively.

2.1 RPI Plasmagrams

Figures 2 and 3 show RPI plasmagrams where the signals are received on the same antenna used for pulse transmissions, namely the X antenna, and Figure (4) shows the N_e information derived from one of these cases. Figure 5 presents resonances observed on the Z antenna, following X-antenna pulsed transmissions, both before and during the large magnetic storm of 31 March 2001. Figures 6 and 7 provide different 3-antenna representations of the magnetic-storm example of Figure 5. Figure 8 overlays the magnetospheric resonance observations of Figures 2, 3 and 5b onto earlier topside ionospheric resonance observations for comparison. The frequency step size was 0.6 kHz in Figure 2 and 0.3 kHz (equal to the RPI bandwidth) in Figures 3 and 5. The labels on the plasmagram figures were based on self-consistent identifications of the resonant and cutoff features. The first step in this identification is to use the Tsy 96-1 model f_{ce} value [*Tsyganenko*, 1995; *Tsyganenko*, 1996; *Tsyganenko and Stern*, 1996], displayed in the lower right-hand corner of each figure, as a guide to identify candidate nf_{ce} resonances. These observed resonances are then used to obtain the best f_{ce} value to use for the plasmagram. For greater accuracy, the gradient of f_{ce} during the time interval of the plasmagram recording should be considered. The model f_{ce}, after correction based on the resonance scaling, is used in this case. The next step is to use the non-nf_{ce} resonances to yield a self-consistent determination of f_{pe} based on the discussion in Section 1.

Figure 2 corresponds to one of the polar-cap plasmagrams used in Figure 5 of Reinisch et al. [2001a]. It was recorded during an outbound pass after crossing the plasmapause and corresponds to the case $f_{pe}/f_{ce} = 0.981 \pm 0.003$. This value was obtained from the n = 2 & 3 nf_{ce} resonances to determine that the Tsy 96-1 model was high by 2.1 ± 0.2%, at the time and location of the recording of this plasmagram, and that $f_{ce} = 23.81 \pm 0.05$ kHz (or, from (1), $|\mathbf{B}| = 850 \pm 2$ nT). This value corresponds to the plasmagram sweep-time of the resonance at 23.7 ± 0.3 kHz. This time was selected because the observed resonance at that time corresponds to the average value calculated for fpe (23.3(5) ± 0.2 kHz or, from (2), $N_e = 6.8 \pm 0.2$ cm^{-3}) based on the observed features attributed to $f_{uh} = 33.1 \pm 0.1$ kHz and $f_x = 38.4 \pm 0.1$ kHz using (3) & (5). These calculations assume that the plasma conditions did not change significantly during the 12 s that elapsed between the recording of f_{pe}, f_{uh} and f_x. This assumption appears justified in this case in view of the good agreement between the two independent methods of determining f_{pe} from f_x and f_{uh} and the observed resonance attributed to the overlapping of the f_{pe} and f_{ce} resonances. Additional confidence in this interpretation is obtained from the observed locations of the Q2 (49.2 ± 0.2 kHz) and the Q3 (71.4 ± 0.2 kHz) resonances corresponding to normalized (by $f_{ce} = 23.81 \pm 0.05$ kHz) values of 2.07 ± 0.02 and 3.00 ± 0.2, respectively. These values are in fairly good agreement with those expected for the case of $f_{pe}/f_{ce} = 0.981 \pm 0.003$ (2.10 ± 0.1 and 3.05 ± 0.2, respectively, based on the equations used to generate the Q curves of Figure 1). Between f_{pe} and f_{uh}, strong signal returns are observed that have been identified as the f_{DNT} resonance. It appears to have two components; the lower-frequency one is broad and centered on 26.1 kHz while the higher-frequency one is narrow and of shorter duration at 27.6 kHz.

Figure 3 illustrates a rare example where both the Z and X mode cutoffs, as well as multiple resonances dependent on Ne and $|\mathbf{B}|$, were captured on a single high-resolution (frequency stepping interval = 300 Hz) plasmagram. In this case, the f_{pe}, f_{uh}, f_{Q3} and the $4f_{ce}$ resonances were also recorded. An inspection of the cutoff and resonant frequencies (see caption) indicated that a consistent interpretation was not possible with fixed values for f_{pe} and f_{ce}. A consistent interpretation was possible, however, by assuming a strong f_{pe} gradient which would be expected based on the location of IMAGE at the time of the recording, namely, in the vicinity of the plasmapause during an outbound pass. The first step in interpreting this record was to determine f_{ce} from the observed value of $4f_{ce}$ and using it to calibrate the Tsy 96-1 model. The model was found to be high, from this and two previous plasmagrams, by 0.3 ± 0.3%. Using this calibrated model, f_{pe} values were found to be 176.6 ± 0.2, 169.9 ± 0.1, 167.6 ± 0.2, 164 ± 1 and 164.1 ± 0.4 kHz from f_z (and (6)), f_{pe}, f_{uh} (and (3)), f_{Q3} (and Figure 1) and f_x (and (5)), respectively.

The above values, after being converted to N_e using (2), are plotted in Figure 4a against the corresponding IMAGE L value at the time of each cutoff or resonance observation. Also plotted are the N_e values deduced from adjacent RPI sounding programs of lower frequency resolution (activated every 4 min) and from adjacent RPI passive dynamic-spectra programs (recorded every 2 min) [*Reinisch et al.*, 2001a]. (The adjacent RPI sounding programs of high frequency resolution, as used to generate Figure 3, did not contain resonances or cutoffs that could be used to deduce f_{pe}.) Straight dashed lines connect the dynamic-spectra values. These values correspond to local intensity peaks and the error bars extend further in the direction of lower N_e based on RPI active/passive comparisons. These comparisons indicate that the dynamic-spectra intensity peaks can

range from agreement with f_{pe} to about 5% above f_{pe} when $f_{pe}/f_{ce} \approx 4$; when $f_{pe}/f_{ce} < 3$ the differences can be much larger, approximately ± 20% [*Benson et al.*, 2002]. The error bars were based on the former values and are thus more appropriate for the lower L values since the estimate for f_{pe}/f_{ce} ranged from 4.1 to 1.5 between the extreme left and right dynamic-spectra values in Figure 4a. While the observed N_e gradient is large, it does not qualify as a well-defined plasmapause based on the criteria of *Carpenter and Anderson* [1992] that the plasmapause scale length Δpp (the distance in L value over which the density drops by an order of magnitude) ≈ 0.1. Not only is the observed gradient less in this case, it is also not possible to fit the data to the right of the change in slope, which occurs between L = 3.90 and 3.98, with a linear decrease in log N_e. This point is illustrated by the changing Δpp values calculated between the indicated pairs of dynamic-spectra N_e values in Figure 4a.

The portion of Figure 4a containing the high-resolution sounding measurements is expanded in Figure 4b. Here the resonance or cutoff frequencies used to derive the N_e values are identified. Straight lines connect these values except for the one deduced from the Q3 resonance. It is not connected to the other values because it can lead to considerably lower values of N_e if there are departures from a Maxwellian electron-velocity distribution (see discussion below pertaining to Figures 6 & 7 and Section 3.5). In this case, it is only low (relative to the f_{uh} to f_x N_e line segment corresponding to an IMAGE motion of approximately 75 km) by 2 ± 1%.

Clear X and/or Z mode cutoffs, as displayed in Figures 2 and 3, are not always present and the spectral identification is then based solely on the stimulated plasma resonances. This situation is particularly true in the distant magnetosphere where N_e and the N_e gradients are very low. Figure 5 presents two such plasmagrams recorded near apogee, one before and one during the large magnetic storm of 31 March 2001. The plasmagram in Figure 5a was recorded at a geocentric radial distance of 8.0 R_E as IMAGE was descending from apogee and it corresponds to the pre-storm conditions on 30 March 2001. It shows nf_{ce} resonances with n = 2-14 but does not reveal other plasma resonances or wave cutoff effects that can be used to make reliable f_{pe} (and thus N_e) determinations. Within the hour, the cusp was encountered and such determinations were made [*Osherovich et al.*, 2001]. The five highest nf_{ce} resonances observed in Figure 5a (less chance for frequency-shift contamination on these high-order harmonics due to the Qn resonances) yielded f_{ce} = 3.275 ± 0.005 kHz (|**B**| = 117.0 ± 0.2 nT). The Tsy 96-1 model, corresponding to the time of the $12f_{ce}$ resonance, was in fairly good agreement with this observation (the model was low by 2.1 ± 0.2%). The lack of an f_{uh} resonance in Figure 5a implies that $f_{pe}/f_{ce} < 1.5$.

The magnetospheric conditions were considerably different during the recording of the plasmagram in Figure 5b on 31 March 2001 due to the magnetic storm. At this time IMAGE was at 6.8 R_E and was approaching apogee. The magnetic field had increased, so that nf_{ce} resonances with n only up to 6 were present in the observed frequency range, and resonances other than the nf_{ce} resonances were clearly present so that f_{pe} (and thus N_e) could be determined. These conditions persisted for hours on this day enabling f_{pe} and f_{ce} to be determined along the apogee portion of the orbit (except when IMAGE penetrated into the magnetosheath and nf_{ce} resonances could not be identified)

[*Osherovich et al.*, 2001]. In Figure 5b, f_{pe}/f_{ce} was determined to be $(18.0 \pm 0.1)/(7.96 \pm 0.01) = 2.26 \pm 0.2$ (see discussion below).

2.2 Normalized 3-Antenna Representations

Plasma resonances are often more pronounced in the recent RPI data on the shorter Z antenna (where "recent " is defined as after 29 March 2001 when the Z-channel receiver gain was significantly decreased). This difference is often most noticeable at higher frequencies and may be due to the more sensitive reception, by the long spin-plane antennas, of waves of natural origin propagating in the free-space O and X modes above f_{pe} and f_x, respectively. When trying to interpret complex plasmagrams such as the one displayed in Figure 5b, however, it is often very helpful to make use of the data from all three RPI receiving antennas. The approach we use is to normalize each frequency step during the sounder sweep by the best estimate for f_{ce} as determined from the observed nf_{ce} resonances. We then make two different data presentations, for each of the three antennas, as a function of the now-normalized sounder frequency. One presentation compares the mean of the signal amplitudes from the first ten range bins with the mean amplitude of all the range bins (Figure 6). A significant amplitude separation between the two curves clearly indicates sounder-stimulated resonant phenomena which are more intense at smaller virtual ranges. Similar amplitudes for the two curves indicate a strong sounder-stimulated response over the entire listening range, the reception of waves of non-sounder origin or interference. The other presentation is in the standard plasmagram format with the exception that the signal-amplitudes are displayed as color-coded contours (Figure 7). It allows a valuable comparison of the complete plasmagram information, i.e., all range bins, on all the antennas. This comparison aids in the detection of resonances that may appear on only one or two antennas, and in the inspection of resonance characteristics, e.g., time durations, floating nature, etc., which can have significant variations among the three receiving antennas.

The normalization in Figures 6 and 7, where the Z-components correspond to the data of Figure 5b, was based on $f_{ce} = 7.96$ kHz ($|\mathbf{B}| = 284$ nT) which corresponds to the mean of the values for the 2 and $3f_{ce}$ resonances. This value was used, rather than one based on the higher harmonics, because it appeared to be the most appropriate for the suspected region of f_{pe} and f_{uh} (since there was evidence of a significant gradient in f_{ce}) and the 2 and $3f_{ce}$ resonances in Figure 5 had well-defined peaks that were not affected by Qn resonances.

The labels on Figures 6 and 7 indicate the observed value of $f_{pe} = 18.0 \pm 0.1$ kHz and the calculated values (based on this value and $f_{ce} = 7.96 \pm 0.01$ kHz) for the D1, D1+, uh, Q2, Q3, Q4, Q5 and Q6 frequencies (11.37 ± 0.04, 13.88 ± 0.04, 19.7 ± 0.1, 20.81 ± 0.08, 26.19 ± 0.06, 33.13 ± 0.06, 40.61 ± 0.06 and 48.32 ± 0.07 kHz, respectively). The difference between the labels in these figures and those in Figure 5 is that all of the Figure 5 labels identify observed features, whereas the labels on Figures 6 and 7 (except for f_{pe}) correspond to calculated values.

While the calculations provide confidence in the resonance identifications, definite differences between the observed and calculated values are apparent. For example, the Q's are observed at frequencies slightly lower than expected for a Maxwellian plasma and suggest a departure from such a distribution. The calculated f_{uh} and f_{Q2} straddle an

intense long-duration feature. Considering the intensity, duration and frequencies of the Q3 and Q4 resonances, the greatest intensity and duration of this intense combined feature is likely due to Q2 with the f_{uh} resonance contributing to it's lower-frequency edge (see the labels at the top of Figure 5b and the calculated values indicated on Figures 6 and 7). The calculated frequencies for the D1 and D1+ resonances correspond to the high-frequency edges of the intense long-duration broadband features observed below f_{pe} and between f_{ce} and 2 f_{ce} on the Z-antenna data of Figures 6 & 7. They coincide with the peaks in the mean signal amplitude of all range bins for the X & Y antenna D1 and D1+ resonance data (see the black curves of Figure 6) and with the similar peaks for the first 10 range bins for all but the D1+ resonance where the calculated and the observed peaks are separated by one frequency step in the X-antenna data (see the red curves of Figure 6). The presentation of Figure 7 indicates that these calculated frequencies agree best with the D1 and D1+ signals received in the highest range bin numbers for the X and Y antenna data.

Other interpretations are possible but they are considered less likely to represent a proper identification. For example, if the resonance at 18 kHz is identified as f_{uh}, then f_{pe} nearly coincides with $2f_{ce}$ and the calculated and observed D1 and D1+ resonances are still in satisfactory agreement with the observed resonances (but tending toward the low-frequency sides) but the calculated f_{Q2} is at the low-frequency side of the broadband long-duration feature that includes 20 kHz in Figure 5b (while the calculated f_{Q3} and f_{Q4} are on the high-frequency sides of their respective resonances), the broadband nature of this feature would have to be explained solely on the basis of the Q2 resonance (not consistent with other plasmagrams of this series) and there would be a large frequency separation between f_{uh} and f_{Q2} (again, not consistent with neighboring plasmagrams). If the long-duration feature that includes 20 kHz in Figure 5b is considered to be a combined f_{pe}, f_{uh} and Q2 resonance, then the strong resonance at 18 kHz has no interpretation, and the discrepancy between the observed and calculated Dn and Qn resonances, as indicated in Figures 6 & 7, increases. The first of these two alternative interpretations leads to f_{pe} = 16.1 kHz and the second to f_{pe} = 19.5 kHz. Relative to the original f_{pe} = 18.0 kHz interpretation, they lead to (from (2)) N_e values that differ by -20 and +17%, respectively.

There are some less-prominent features in Figures 5, 6 and 7 that have not been labeled. Near 35 kHz in Figure 5b there is a long-duration weak signal that appears to float away from the zero virtual-range baseline. (Signals that appear at multiples of 5 kHz must be treated with some caution because interference lines are occasionally encountered at these frequencies in the Z antenna data.) It appears at $4.4f_{ce}$ as a peak in the black curve in the Z-data of Figure 6 and as a weak floating signal in the Z-data of Figure 7. Such signals, (of considerably greater amplitude and not always appearing at a multiple of 5 kHz) occurring in the frequency range above f_{uh} and between the nf_{ce} harmonics at frequencies higher than the calculated f_{Qn} frequencies of Figure 1, are fairly common. There is a weak short-duration signal near 9.6 kHz in Figure 5b, that appears more prominently at $1.2f_{ce}$ in the Y-antenna data of Figures 6 and 7, that corresponds to a resonance known to occur in the topside ionosphere near $f_{uh}/2$ when $f_{uh}/2 \approx f_{pe} - f_{ce}$ that has been called the "floating" resonance because it is often observed to be initiated after a short delay time following the sounder pulse [*Hagg et al.*, 1969; *Hagg and Muldrew*, 1970]; it is typically observed when f_{pe}/f_{ce} is in the range from 1.85 to 2.35 [*Benson*,

1982]. Even though it is called the "floating resonances" (based on its appearance on ionospheric topside ionograms), it has no relation to the higher-frequency resonance described above which is observed to "float" on the RPI plasmagram.

All of the plasma resonances displayed on the RPI plasmagrams in Figures 3 and 5 are present on at least two consecutive frequency channels. Recall that the frequency stepping was equal to the RPI 300-Hz receiver bandwidth in these cases. The resonances in Figure 3, corresponding to a steep plasmapause N_e gradient, are observed to be of shorter duration and narrower bandwidth than those in Figures 5a and 5b, which were recorded near apogee. For example, compare the $4f_{ce}$ resonance in Figure 3 (labeled "4" at the top) with the lower-order nf_{ce} resonances in Figure 5a or with the n = 2 & 3 nf_{ce} resonances in Figure 5b (which are observed without overlapping adjacent resonances). Also, compare the f_{pe} resonances in Figures 3 and 5b. In Figure 5a, the lower-order nf_{ce} resonances have widths of up to 5 or 6 frequency channels when the virtual range is about 0.5 R_E. Similar widths are observed for the f_{pe} and $3f_{ce}$ resonances in Figure 5b. At greater virtual ranges (beyond about 1.0 R_E), the resonances are typically confined to about two frequency channels.

Figure 8 compares the RPI/IMAGE magnetospheric plasma-resonance observations, presented in Figures 2, 3 and 5b, with earlier Alouette-2 and ISIS-1 ionospheric topside-sounder plasma-resonance observations. The Q2 and Q3 resonances observed for the f_{ce}/f_{pe} = 0.98 case of Figure 2 are in good agreement with the ionospheric Qn observations, whereas only the higher-frequency component of the two features in Figure 2 identified as the DNT resonance agrees with the ionospheric observations of this unexplained feature. The magnetospheric Q3 resonance at f_{pe}/f_{ce} = 3.4 (from Figure 3) is in good agreement with the ionospheric observations. The magnetospheric Qn resonances for the f_{ce}/f_{pe} = 2.26 case of Figure 5b during the magnetic storm of 31 March 2001 appear below the ionospheric Qn resonances, whereas the Dn resonances agree with the ionospheric observations. This particular case is from the first of 55 high-resolution plasmagrams recorded during this period. These plasmagrams, many showing similar Dn & Qn spectral characteristics, allowed variations in f_{pe}/f_{ce} to be accurately determined and to be compared with solar-wind parameters [*Osherovich et al.*, 2001].

3. Discussion

Since the RPI transmissions stimulate spectra of wave cutoffs and plasma resonances that are very similar to those observed over several decades by rocket and satellite-borne radio sounders in the ionosphere, a brief review of the observed spectral characteristics of these features as observed in the ionosphere, and how the RPI magnetospheric observations relate to them, is in order. This review and comparison is of particular importance to the concept that the main (though not the only) controlling factor of the spectra of sounder-stimulated plasma resonances is the plasma parameter f_{pe}/f_{ce}. Thus similar spectra are expected even under conditions where the absolute values of N_e and the electron temperature T_e differ greatly as long as this plasma parameter is similar under the different conditions. This prediction was made in regard to the Dn resonances by *Osherovich* [1989]. Evidence in support of this prediction has been provided based on ionospheric topside sounding (see Section 3, reason 4 of *Benson et al*. [2001b]),

relaxation sounding in Jupiter's Io plasma torus [*Osherovich et al.*, 1993] and in the terrestrial magnetosphere by the present work. Such spectral similarities, for similar f_{pe}/f_{ce} values, provide confidence in the accurate extraction of geophysical parameters from RPI-stimulated plasma resonance data.

3.1 Bandwidths of Sounder-Stimulated Plasma Resonances

High frequency-resolution rocket sounder experiments indicate that the bandwidths of the nf_{ce} resonances are of the order of a few kilohertz or less [*Higel et al.*, 1972; *McAfee et al.*, 1972; *Bitoun et al.*, 1975]. These observations are consistent with the electrostatic-echo interpretation for these resonances [*Muldrew*, 1972a; *Bitoun et al.*, 1975] since the received signals from a relatively-wide spectrum of the transmitted pulse appear at different delay times within the relatively-broad receiver bandwidth [*McAfee et al.*, 1972]. The bandwidth of the f_{uh} resonance is broader (sometimes signals appeared to extend over 100 kHz) but a well-defined peak was often observed that varied in frequency with delay time as predicted by the wave-propagation interpretation of the resonance [*McAfee et al.*, 1972]. Similarly, the f_{pe} resonance is broader (sometimes ~ 10 kHz) and the broadening has been attributed to N_e irregularities [*Higel*, 1978b]. The narrow bandwidth (relative to that of the transmitter and receiver) of the above resonances is also indicated by the observed frequency spectrum of the 0.1 ms transmitted pulse on the Alouette-2 resonances [*Benson*, 1969; *Warnock*, 1969].

Even though the above investigations indicated that the inherent bandwidths of the nfce, fpe and (often) the f_{uh} sounder-stimulated plasma resonances were much less than the Alouette-2 sounder-receiver 3 dB bandwidth of 37 kHz, the effective bandwidth for the detection of these resonances on Alouette 2 was determined to be approximately double the receiver's bandwidth [*Benson*, 1975]. The RPI observations of Figures 2-5 indicate that the magnetospheric resonances (presumably also of a narrowband nature) are also (often) observed over a wider frequency range than the receiver bandwidth. The plasmagrams in these figures were produced from operating programs that either had frequency steps equal to the RPI receiver 3 dB bandwidth of 0.3 kHz or equal to twice this value. While the higher-order nf_{ce} resonances in Figure 5a are observed to have a bandwidth of this order or slightly greater, the lower-order resonances in this figure and those in Figure 5b appear over a much wider frequency range. For example, the 2 and $3f_{ce}$ and other well-defined single resonance in Figure 5b, such as those at f_{pe} and f_{Q3}, suggest an effective bandwidth for strong resonant phenomena, i.e., corresponding to virtual ranges of a few tenths R_E, to be at least five 0.3 kHz frequency steps. The 2fce resonance in Figure 2 extends over three 0.6 kHz frequency steps. Thus the effective bandwidth of strong magnetospheric resonances is 5 to 6 times the 0.3 kHz receiver bandwidth. When expressed in terms of the inverse of the width of the transmitted pulse τ (= 100 μs for Alouette 2 and 3.2 ms for RPI) then the effective bandwidths for resonance detection in the ionosphere and the magnetosphere are fairly similar (approximately $8/\tau$ for Alouette 2 and $5/\tau$ to $6/\tau$ for RPI). Thus RPI sounding programs with frequency step sizes approaching 2 kHz should still be able to detect some plasma resonances that will aid in the inversion of reflection traces to N_e profiles.

In analogy to Alouette 2, and considering that some of the RPI resonances are only observed on one frequency step, the natural bandwidths for the sounder-stimulated magnetospheric plasma resonances are of the order of 300 Hz or less.

3.2 Intensities and Time Durations of Sounder-Stimulated Plasma Resonances

Many of the ionospheric sounder-stimulated resonances display dramatic changes in amplitude, time duration, amplitude modulation, or frequency structure as plasma conditions change. The f_{uh} resonance changes from strong to weak as plasma conditions change from $f_{uh} < 2f_{ce}$ to $f_{uh} > 2f_{ce}$ [*Fejer and Calvert*, 1964; *Benson*, 1972b; *McAfee et al.*, 1972], the f_{pe} resonance changes from weak to strong as plasma conditions change from $f_{pe} < f_{ce}$ to $f_{pe} > f_{ce}$ [*McAfee*, 1970; *Benson*, 1971], and the nf_{ce} resonances change from weak to strong as plasma conditions change from $f_{pe} < nf_{ce}$ to $f_{pe} > nf_{ce}$ [*Higel et al.*, 1972; *Benson*, 1974]. Similar behaviors for the f_{pe} and f_{uh} resonances were observed in the relaxation-sounder data from the higher-altitude Viking satellite [*Perraut et al.*, 1990]. Recalling these characteristics is of value when attempting to interpret magnetospheric sounder-stimulated plasma resonances since the relevant RPI observations are consistent with the ionospheric observations. For example, the f_{uh} resonance in Figure 2 ($f_{uh} < 2f_{ce}$) is observed to be much stronger than the f_{uh} resonance in Figure 3 ($f_{uh} > 2f_{ce}$), the f_{pe} resonance in Figure 5b ($f_{pe} > f_{ce}$) is stronger than the combined f_{pe} and f_{ce} resonance ($f_{pe} < \approx f_{ce}$) of Figure 2, and of the two nf_{ce} resonances near f_{pe} in Figure 5b, $2f_{ce}$ (observed below f_{pe}) is stronger than $3f_{ce}$ (observed above f_{pe}). Note that even though the plasma conditions of Figure 3 correspond to the weak form of f_{uh} and the strong form of f_{pe} ($f_{uh} > 2f_{ce}$ and $f_{pe} > f_{ce,}$ respectively), in this example the f_{uh} resonance has a much longer time duration than the f_{pe} resonance (the f_{pe} resonance, however, is of greater intensity at shorter time durations, e.g., corresponding to virtual ranges less than about 1 R_E). The plasma conditions of Figure 5b also correspond to the weak and strong forms of f_{uh} and f_{pe}, respectively. In this case, however, f_{ce} is lower (relative to Figure 3) by a factor of 6. Under such low f_{ce} conditions, the f_{uh} resonance is often observed on RPI plasmagrams to be merged with the lowest order Qn resonance (as in figure 5b), the f_{pe} resonance, or both.

The observed time durations of most of the resonances stimulated by ionospheric topside sounders have been well explained in terms of electrostatic echoes [*Muldrew*, 1972a]. In the magnetosphere, on the other hand, unpublished work by J. Bitoun predicts that the nf_{ce} resonances should have time durations of ~ 15 ms yet they can persist for more than 100 ms (see, e.g., *Etcheto et al*. [1983], *Canu* [2001a] and Figure 5 of the present paper where 100 ms corresponds to 2.35 R_E of virtual range). Similarly, the Qn resonances are often observed to have extremely long time durations, as in Figure 5b, much longer than observed in the topside ionosphere. Since the time durations of ionospheric sounder-stimulated plasma resonances attributed to oblique echoes are extremely sensitive to local N_e and **B** gradients, it is likely that the long time durations observed for the corresponding RPI- stimulated plasma resonances are due to the much longer magnetospheric distances required to achieve the required change in parameters to produce echoes.

3.3 |B| from nf_{ce} Plasma Resonances

Observations of the nf_{ce} resonant frequencies, based on rocket and satellite-borne sounders, indicate agreement with magnetic-field model predictions within the accuracy of the models (~ 0.1%) [*Benson*, 1972a; *Higel et al.*, 1972; *McAfee et al.*, 1972] with the possible exception of the $2f_{ce}$ resonance, when $2f_{ce} \approx f_{uh}$, where frequency deviations of the order of 1% have been reported [*Benson*, 1972a]. As indicated in the discussion pertaining to Figure 5, the magnetospheric nf_{ce} resonant frequencies stimulated by RPI are consistent with one another to an accuracy of the order of 0.1% when strong |**B**| gradients are not present. Under such conditions, and when high order nf_{ce} resonances are present (e.g., $n \geq 5$), |**B**| can be determined from (1) with an accuracy better than 0.1% even on spacecraft (such as IMAGE) that do not carry a scientific magnetometer.

3.4 N_e from the f_{pe} and f_{uh} Plasma Resonances and the em Wave Cutoffs

The N_e can be determined directly from f_{pe} (from (2)) or, once f_{ce} is determined from the nf_{ce} resonances as described above, from f_{uh}, f_x or f_z using (3), (5) or (6), respectively. The f_{pe} and f_{uh} resonances form a pair with f_{uh} as the high-frequency component as defined by (3). Even when $f_{uh} > 2f_{ce}$ (the weak form of the f_{uh} resonance on ionospheric topside-sounder ionograms), the f_{uh} resonance can have a time duration greater than that at f_{pe} which often, but not always, corresponds to a strong resonance. Often, the f_{uh} resonance is observed as part of a strong long-duration signal consisting of a combined response with the lowest order Qn resonance. Independent f_{pe} determinations are possible when wave cutoffs are present. These cutoffs, which correspond to clear signal returns projected to zero virtual range, are almost always observed for the X and Z traces but seldom for the O trace on ionospheric topside ionograms [*Hagg et al.*, 1969; *Jackson*, 1969]. When magnetospheric reflection traces are observed by RPI, wave cutoffs are also observed more often on X and Z than on O as illustrated in Figures 2 and 3. In the case of Figure 3, where multiple resonances and cutoffs were observed on the same plasmagram, four independent N_e measurements could be made with high confidence (ΔN_e ranged from ~ 0.1 to 1%). The departure of these values from a single straight line on the N_e vs. L (log/linear) plot of Figure 4b illustrates the irregular nature of the plasmapause boundary region based on *in situ* IMAGE/RPI observations. Plasmapause N_e irregularities are also routinely inferred from IMAGE/RPI remote-sounding observations [*Carpenter et al.*, 2002].

3.5 N_e from the Qn Resonances

Warren and Hagg [1968] concluded that the Qn resonances are observed at the expected frequencies for a Maxwellian plasma in the ionosphere within the experimental error. They were observed to be weak or absent in the Viking relaxation-sounder data when $f_{pe} < f_{ce}$ [*Perraut et al.*, 1990]. In addition to the main resonances, upper and lower subsidiary Qn resonances have been observed by the Alouette-2 topside sounder in the ionosphere [*Benson*, 1982]. Frequency splitting of the Qn resonances has also been observed in the magnetosphere by relaxation sounders on GEOS 1 [*Higel*, 1978a; *Belmont*, 1981], ISEE 1 [*Trotignon et al.*, 1986] and the Cluster spacecraft [*Canu et al.*,

2001; *Trotignon et al.*, 2001]. As pointed out in the discussion near the end of Section 2, pertaining to some less-prominent features in Figures 5b, 6 and 7, additional resonances are sometimes observed above f_{uh} and between nf_{ce} at frequencies above the calculated Qn frequencies based on a Maxwellian distribution. These resonances can be more prominent than shown in these figures and do not always float away from the zero virtual-range base line. Such floating of the Qn resonances is commonly observed with ionospheric topside sounders and has been attributed to the time required for the ion sheath around the antenna (resulting from the sounder pulse) to collapse so that waves with wavelengths comparable to the sheath radius can reach the antenna [*Muldrew*, 1972b].

It is important to determine how well f_{pe} deduced from the Qn resonances (and f_{ce}) compares with the sounder-stimulated f_{pe} resonance because this method has been reported to be used to deduce N_e in relaxation-sounder data when no f_{pe} resonance is observed [*Trotignon et al.*, 2001]. The RPI-stimulated Qn resonant frequencies superimposed on the ionospheric observations in Figure 8 indicate agreement with the ionospheric observations in the cases corresponding to Figures 2 ($f_{pe}/f_{ce} = 0.98$) and 3 ($f_{pe}/f_{ce} = 3.40$) (in spite of the slight offset discussed in connection with Figure 4 related to the latter). There is a disagreement, however, in the $f_{pe}/f_{ce} = 2.26$ case corresponding to the data of Figures 5b (same event also shown in Figures 6 and 7). Thus, this case likely reflects a significant departure from a Maxwellian distribution. Such examples are common in the RPI data and have been reported earlier in magnetospheric relaxation sounder data from GEOS 1 & 2 and ISEE 1 [*Belmont*, 1981; *Etcheto et al.*, 1983; *Trotignon et al.*, 1986] and more recently from the Cluster spacecraft [*Canu et al.*, 2001; *Trotignon et al.*, 2001]. Because of this uncertainty introduced into the Qn frequencies by the lack of knowledge of the electron velocity-distribution function, our approach, in general, is to use the Qn resonances to aid in the spectral interpretation of the RPI-stimulated plasma resonances rather than to determine f_{pe}. If only nf_{ce} and Qn resonances can be confidently identified on a plasmagram, however, then the Qn resonances can be used to estimate f_{pe}. The resulting estimate for f_{pe} can be in error by several tens of per cent, however, as illustrated in the data corresponding to Figure 5b where both f_{pe} and Qn resonances are present. In this case f_{pe} was determined to be 18.0 ± 0.1 kHz from the observed resonance identified as f_{pe}. It was also determined from the calculated f_{Q2}, f_{Q3} and f_{Q4} values (based on numerical solutions of the dispersion equation used to derive the curves of Figure 1). The results were found to be low (relative to the fpe resonance) by 6, 17 and 26%, respectively. In terms of N_e, these determinations would lead to values low by 11, 31 and 46%, respectively. (The uncertainty in performing these calculations is greatest for the Q2 resonance since it appears merged with the f_{uh} resonance and it is difficult to accurately determine f_{Q2}.) Thus, this approach of using the Qn resonances to determine N_e must be used with caution if accurate (a few %) values are desired. A parametric study involving different electron velocity distributions is called for in order to obtain an understanding of the relevant physics so that velocity distribution information can be deduced from the Qn resonance spectral signatures.

3.6 N_e from the Dn Resonances

There are two extremely prominent features between f_{ce} and $2f_{ce}$ in Figure 5b in the frequency range below the identified f_{pe} that are consistent with the calculated D1 and D1+ frequencies as indicated by the vertical green lines in Figure 6 and the short tick marks on the top and bottom of each panel in Figure 7. Though the interpretation of such RPI plasmagrams is often not trivial, many examples with Dn resonances have been identified and have been used to provide confidence in the spectral identification of the RPI-stimulated plasma resonances. To date, these resonances have not been reported to be present in the data from magnetospheric relaxation sounders in spite of attempts to detect them on GEOS 1 & 2 and ISEE 1 [*Canu*, 2001a] and on the Cluster spacecraft [*Canu et al.*, 2001]. The agreement between the IMAGE/RPI-observed Dn resonances of Figure 5b (also observed in the 3-antenna formats of Figures 6 and 7) with the ionospheric observations, as indicated in Figure 8, suggests that the RPI observations may shed light on the generation mechanism of these emissions. Five different approaches have been suggested for the Dn generation mechanism as discussed in Section 1 of *Benson et al*. [2001b]. Two placed great emphasis on explaining the sharply enhanced persistence of the D1 resonance (up to 200 times the duration of the sounder pulse) when D1 was observed in a narrow frequency range ($1.5 \leq f_{D1}/f_{ce} \geq 1.63$) [*Oya*, 1971; *Kiwamoto and Benson*, 1979] and two placed great emphasis on explaining the spectral properties of the Dn resonances [*Oya*, 1971; *Osherovich*, 1987]. The mechanism of *Osherovich* [1987] was expanded to include all the Dn spectral components as described in equations (7) - (9). These equations, which correspond to eigenmodes of cylindrical-em plasma oscillations, provide additional independent means of determining f_{pe}, and hence N_e, once f_{ce} is determined. The hybrid nature of (8) & (9) provide a valuable spectral signature that ads confidence to the determination of f_{pe}.

3.7 Qn Components of Natural Origin

There is evidence that there may be a natural, i.e., non-sounder stimulated, component to the Qn resonances. For example, the Q2 and Q3 resonances in Figure 5b show very little change in intensity over the entire listening range of the record. This behavior, which is also evident in Figures 6 (where there is only a slight separation between the red and black curves) and 7, could either indicate that the resonances are of extremely long time duration or that part of the signals are due to natural emissions at the Qn frequencies. Evidence for such natural emissions has been clearly presented during alternate active/passive operations of the relaxation sounders on GEOS 1 [*Christiansen et al.*, 1978], GEOS 2 [*Etcheto et al.*, 1983] and Cluster [*Canu et al.*, 2001] and has been inferred in the interpretation of passive AMPTE/IRM spectra [*Benson et al.*, 2001b]. *Christiansen et al*. [1978] argue for an incoherent generation mechanism, involving a small population of non-thermal high-energy electrons, for these natural (as opposed to sounder-stimulated) Qn waves.

3.8 Dn Components of Natural Origin and FAI

The strong response for the D1 resonance at all delay times (and to a lesser extent with the D1+ resonance) in Fig 5b (see Figures 6 & 7 also) suggests a possible component due

to natural emissions, in addition to the sounder-stimulated responses, for the Dn resonances. The interpretation that the strong signal identified as D1 has a sounder-stimulated component is supported by the X & Y channels of Figures 6 & 7 where separations between the red and black curves are apparent (Figure 6) and signal enhancements are apparent in the first few range bins (Figure 7). A natural contribution for the Dn resonances has been suggested earlier and they have been related to the well-known magnetospheric "$(n + 1/2)f_{ce}$" emissions [*Fredricks*, 1971; *Oya*, 1972; *Benson and Osherovich*, 1992; *Benson et al.*, 2001b].

The cylindrical structures involved in the oscillations attributed to the Dn resonances (see Section 3.6) are considered to be FAI which are common in the ionosphere, as indicated by their spectacular signatures due to wave scattering and ducting on topside ionograms [*Muldrew*, 1963; *Muldrew and Hagg*, 1969; *Dyson and Benson*, 1978; *Benson*, 1985; *James*, 1989], and in the magnetosphere as indicated by similar signatures on RPI plasmagrams of wave scattering, such as in Figure 3 (Z-mode scattering) and near the plasmapause [*Carpenter et al.*, 2002; *Fung et al.*, 2002]. They also may be responsible for the hemisphere-to-hemisphere wave propagation guided along the magnetic-field direction as reported by *Reinisch et al*. [2001b] and *Fung et al*. [2002]. There is also evidence that in addition to these FAI being commonly generated by natural processes, they can be either stimulated or enhanced by the sounder pulse [*Benson*, 1997]. Thus, if the *Osherovich* [1987] mechanism is the correct interpretation of the Dn resonances, and if the claimed relationship between the Dn resonances and the magnetospheric narrowband "$(n + 1/2)f_{ce}$" emissions can be confirmed, then the occurrence of such emissions may provide a sensitive passive indicator of magnetospheric FAI.

3.9 Unexplained Resonances

In addition to the unexplained DNT resonance between f_{pe} and f_{uh} illustrated in Figure 2, the resonance near $f_{uh}/2$ when $f_{uh}/2 \approx f_{pe} - f_{ce}$ as discussed in connection with Figures 5, 6 and 7 and the additional resonances above f_{uh} discussed in Section 3.5, there are numerous short-duration resonances attributed to nonlinear plasma processes that are observed by ionospheric topside sounders. These resonances, observed at the harmonics and sum and difference frequencies of the principal resonances, are restricted to the plasma conditions $f_{pe} < 2f_{ce}$ ($f_{pe}/f_{ce} < 3^{1/2}$) [*Benson*, 1982]. The harmonic of the "floating" resonance occurs outside this range, namely when $1.85 < f_{pe}/f_{ce} > 2.35$. A thorough investigation of the IMAGE/RPI plasmagrams to detect the presence of these resonances has not been performed.

4. Summary

The spectral signatures of RPI-stimulated plasma resonances in the magnetosphere from the plasmapause to near the magnetopause are found to be remarkably similar to the spectral signatures of topside-sounder stimulated plasma resonances in the ionosphere from 500 to 3500 km. This similarity is found despite vast differences in the magnitude of N_e and T_e in the two regions. The main controlling factor of the spectral features is the plasma parameter f_{pe}/f_{ce} which often has similar values in the two regions. The main spectral deviations between the two regions are in the Qn resonances observed between the nf_{ce} harmonics and above f_{uh}. In the magnetosphere, the frequencies of these

resonances can deviate significantly from their expected values based on a Maxwellian electron-velocity distribution. The frequency of the magnetospheric Dn resonances, observed between the nf_{ce} harmonics and below f_{pe}, do not appear to be significantly shifted from the frequencies of their ionospheric counterparts observed under similar f_{pe}/f_{ce} conditions. This observation suggests that the eigenmodes of the cylindrical plasma oscillations, presumably FAI, attributed to these resonances are much more sensitive to the ambient f_{pe}/f_{ce} value than to characteristics of velocity distribution function. The analysis technique of comparing signal-amplitude averages over different rang-bin intervals provides additional evidence that the Dn, as well as the Qn, resonances can have components due to natural magnetospheric emissions. Both the sequence of Qn and Dn resonances, and the Z and X mode em wave cutoffs if observed, are valuable in confirming the identity of the f_{pe} and/or the f_{uh} RPI-stimulated plasma resonances once f_{ce} is determined from the RPI-stimulated nf_{ce} resonances. When RPI is operating in a resonance mode, and such confident spectral identification can be performed, f_{ce} and f_{pe} can often be determined to within an accuracy of the order of 0.1 and 1%, respectively. The resulting accuracy in determining N_e (uncertainty approximately twice that of f_{pe}) is difficult to achieve by any other technique in the low-density ($N_e \sim 1$ cm^{-3}) magnetosphere. Even a misidentification of f_{pe} for f_{uh}, or *visa versa*, would lead to uncertainties in the deduced f_{pe} of only around 10% (still a competitive procedure for determining low magnetospheric N_e values). Magnetospheric N_e determinations based solely on f_{ce} and the sequence of Qn resonances can lead to significantly higher uncertainties. The long time durations (relative to their ionospheric counterparts) for the magnetospheric plasma resonances attributed to the reception of RPI-stimulated plasma waves may be due to the great distance required to achieve significant changes in N_e and **B**, i.e., the corresponding gradients are much less in the magnetosphere than in the ionosphere.

Acknowledgements. We are grateful to A. F.-Vinas for the computer code used for the Qn frequency calculations and for helpful discussions to W. Schar for assistance in the data analysis and presentations, and to P. Webb for helpful discussions and assistance in the presentations . The BinBrowser used for the analysis and display of the RPI data was developed by Ivan Galkin and Grigori Khmyrov at UML. Support for B. W. R. was provided by NASA under subcontract 83822 from SwRI.

References

Beghin, C., J.L. Rauch, and J.M. Bosqued, Electrostatic plasma waves and HF auroral hiss generated at low altitude, *J. Geophys. Res.*, *94*, 1359-1379, 1989.

Belmont, G., Characteristic frequencies of a non-Maxwellian plasma: a method for localizing the exact frequencies of magnetospheric intense natural waves near f_{pe}, *Planet. Space Sci.*, *29*, 1251-1266, 1981.

Benson, R.F., Frequency shifts observed in the Alouette II cyclotron harmonic plasma resonances, *Proc. IEEE*, *57*, 1139-1142, 1969.

Benson, R.F., Alouette 2 observations supporting the oblique echo model for the plasma frequency resonance, *J. Geophys. Res.*, *76* (4), 1083-1087, 1971.

Benson, R.F., Frequency shifts of ionospheric nfH resonances, *J. Atm. and Terr. Phys.*, *34*, 1201-1214, 1972a.
Benson, R.F., Ionospheric plasma resonances: Time durations vs. latitude, altitude, and fN/fH, *Planet. Space Sci.*, *20*, 683-706, 1972b.
Benson, R.F., Stimulation of the Harris instability in the ionosphere, *Phys. Fluids*, *17*, 1032-1037, 1974.
Benson, R.F., Ion effects on ionospheric electron resonance phenomena, *Radio Sci.*, *10*, 173-185, 1975.
Benson, R.F., Stimulated plasma waves in the ionosphere, *Radio Sci.*, *12*, 861-878, 1977.
Benson, R.F., Stimulated plasma instability and nonlinear phenomena in the ionosphere, *Radio Sci.*, *17*, 1637-1659, 1982.
Benson, R.F., Field-aligned electron density irregularities near 500 km - Equator to polar cap topside sounder Z mode observations, *Radio Sci.*, *20*, 477-485, 1985.
Benson, R.F., Elusive upper hybrid waves in the auroral topside ionosphere, in *Auroral Plasma Dynamics, Geophysical Monograph 80*, edited by R.L. Lysak, pp. 267-274, American Geophysical Union, Washington, D. C., 1993.
Benson, R.F., Evidence for the stimulation of field-aligned electron density irregularities on a short time scale by ionospheric topside sounders, *J. Atm. and Solar-Terr. Phys.*, *59* (18), 2281-2293, 1997.
Benson, R.F., J. Fainberg, R.A. Hess, V.A. Osherovich, and R.G. Stone, Comment on "Observation of long-duration gyroharmonic resonances: A refutation of the short-duration explanation for interpreting the anomalous URAP sounder spectra observed in the Io torus" by P. Canu, *Radio Sci.*, *36*, 1649-1652, 2001a.
Benson, R.F., J.L. Green, S.F. Fung, B.W. Reinisch, W. Calvert, D.M. Haines, J.-L. Bougeret, R. Manning, D.L. Carpenter, D.L. Gallagher, P.H. Reiff, and W.W.L. Taylor, Magnetospheric radio sounding on the IMAGE mission, *Radio Sci. Bull.*, *No 285*, 9-20, 1998.
Benson, R.F., and V.A. Osherovich, High order stimulated ionospheric diffuse plasma resonances - significance to magnetospheric emissions, *J. Geophys. Res.*, *97*, 19,413-19,419, 1992.
Benson, R.F., V.A. Osherovich, J. Fainberg, A. F.-Vinas, and D.R. Ruppert, An interpretation of banded magnetospheric radio emissions, *J. Geophys. Res.*, *106*, 13,179-13,190, 2001b.
Benson, R.F., P.A. Webb, J.L. Green, and B.W. Reinisch, Relating magnetospheric passive dynamic spectral emission peaks to plasma and upper-hybrid frequencies determined from active RPI sounding on IMAGE, *Eos Trans. AGU*, *83 (19)*, Spring Meet. Suppl., Abstract SM21A-06, 2002.
Bitoun, J., L. Fleury, and B. Higel, Theoretical study of gyroresonances with application to rocket experiments, *Radio Sci.*, *10* (10), 875-889, 1975.
Canu, P., Observation of long-duration gyroharmonic resonances: A refutation of the short-duration explanation for interpreting the anomalous URAP sounder spectra observed in the Io torus, *Radio Sci.*, *36*, 171-181, 2001a.
Canu, P., Reply, *Radio Sci.*, *36*, 1645-1647, 2001b.
Canu, P., P.M.E. Decreau, J.G. Trotignon, and et al., Identification of natural plasma emissions observed close to the plasmapause by the Cluster-Whisper relaxation sounder, *Ann. Geophysicae*, *19*, 1697-1701, 2001.

Carpenter, D.L., and R.R. Anderson, An ISEE/whistler model of equatorial electron density in the magnetosphere, *J. Geophys. Res.*, *97*, 1097-1108, 1992.

Carpenter, D.L., M.A. Spasojevic, T.F. Bell, U.S. Inan, B.W. Reinisch, I.A. Galkin, R.F. Benson, J.L. Green, S.F. Fung, and S.A. Boardsen, Small-scale field-aligned plasmaspheric density structures inferred from RPI on IMAGE, *J. Geophys. Res.*, *107*, in press, 2002.

Christiansen, P., P. Gough, G. Martelli, J.-J. Bloch, N. Cornilleau, J. Etcheto, R. Gendrin, D. Jones, C. Beghin, and P. Decreau, Geos I: Identification of natural magnetospheric emissions, *Nature*, *272* (20 April), 682-686, 1978.

Dyson, P.L., and R.F. Benson, Topside sounder observations of equatorial bubbles, *Geophys. Res. Lett.*, *5*, 795-798, 1978.

Etcheto, J., G. Belmont, P. Canu, and J.G. Trotignon, Active sounder experiments on GEOS and ISEE, in *Active Experiments in Space, Proceedings of an International Symposium held at Alpbach, Austria 24-28 May 1983*, pp. 39-46, European Space Agency, Noordwijk, Netherlands, 1983.

Etcheto, J., and J.J. Bloch, Plasma density measurements from the GEOS-1 relaxation sounder, *Space Science Reviews*, *22*, 597-610, 1978.

Fejer, J.A., and W. Calvert, Resonance effects of electrostatic oscillations in the ionosphere, *J. Geophys. Res.*, *69*, 5049-5062, 1964.

Fredricks, R.W., Plasma instability at (n + 1/2)fc and its relationship to some satellite observations, *J. Geophys. Res.*, *76*, 5344-5348, 1971.

Fung, S.F., R.F. Benson, D.L. Carpenter, J.L. Green, V. Jayanti, I.A. Galkan, and B.W. Reinisch, Guided Echoes in the Magnetosphere: Observations by Radio Plasma Imager on IMAGE, *Geophys. Res. Lett.*, submitted, 2002.

Galkin, I.A., G.Khmyrov, A. Kozlov, B.W. Reinisch, X. Huang, and G.Sales, New tools for analysis of space-bourne sounding data, in *Proc. 2001 USNC/URSI National Radio Science Meeting, July 8-13*, pp. 304, Boston, 2001.

Goertz, C.K., and R.J. Strangeway, Plasma waves, in *Introduction to Space Physics*, edited by M.G. Kivelson, and C.T. Russell, pp. 356-399, Cambridge University Press, New York, 1995.

Hagg, E.L., E.J. Hewens, and G.L. Nelms, The interpretation of topside sounder ionograms, *Proc. IEEE*, *57*, 949-960, 1969.

Hagg, E.L., and D.B. Muldrew, A novel spike observed on Alouette II ionograms, in *Plasma Waves in Space and Laboratory*, edited by J.O. Thomas, and B.J. Landmark, pp. 69-75, Edinburgh University Press, Edinburgh, 1970.

Higel, B., Small scale structure of magnetospheric electron density through on-line tracking of plasma resonances, *Space Sci. Rev.*, *22*, 611-631, 1978a.

Higel, B., Small-scale irregularities of electron density in the F region from f_N resonances observed by a rocket-borne relaxation sounding experiment, *Radio Sci.*, *13*, 901-916, 1978b.

Higel, B., J. Bitoun, and M. Petit, Rocket observations of two waves beating at $3f_H$ resonance, *J. Geophys. Res.*, *77*, 6254-6258, 1972.

Jackson, J.E., The reduction of topside ionograms to electron-density profiles, *Proc. IEEE*, *57*, 960-976, 1969.

James, H.G., Wave propagation experiments at medium frequencies between two ionospheric satellites 3. Z mode pulses, *J. Geophys. Res.*, *84*, 499-506, 1979.

James, H.G., ISIS 1 measurements of high-frequency backscatter inside the ionosphere, *J. Geophys. Res.*, *94*, 2617-2629, 1989.

Kiwamoto, Y., and R.F. Benson, Nonlinear Landau damping in the ionosphere, *J. Geophys. Res.*, *84*, 4165-4174, 1979.

Kurth, W.S., G.B. Hospodarsky, D.A. Gurnett, M.L. Kaiser, J.-E. Wahlund, A. Roux, P. Canu, P. Zarka, and Y. Tokarev, An overview of observations by the Cassini radio and plasma wave investigation at Earth, *J. Geophys. Res.*, *106* (A12), 30239-30252, 2001.

LeSager, P., P. Canu, and N. Cornilleau-Wehrlin, Impact of the Ulysses velocity on the diagnosis of the electron density by the Unified Radio and Plasma Wave sounder in the outskirts of the Io torus, *J. Geophys. Res.*, *103* (A11), 26,667-26,677, 1998.

Lockwood, G.E.K., A ray-tracing investigation of ionospheric Z-mode propagation, *Can. J. Phys.*, *40*, 1840-1843, 1962.

McAfee, J.R., Topside plasma frequency resonance below the cyclotron frequency, *J. Geophys. Res.*, *75*, 4287-4290, 1970.

McAfee, J.R., T.L. Thompson, W. Calvert, and J.M. Warnock, Rocket observations of topside resonances, *J. Geophys. Res.*, *77* (28), 5542-5550, 1972.

Muldrew, D.B., Radio propagation along magnetic field-aligned sheets of ionization observed by the Alouette topside sounder, *J. Geophys. Res.*, *68*, 5355-5370, 1963.

Muldrew, D.B., Nonvertical propagation and delayed-echo generation observed by the topside sounders, *Proc. IEEE*, *57*, 1097-1107, 1969.

Muldrew, D.B., Electron resonances observed with topside sounders, *Radio Sci.*, *7*, 779-789, 1972a.

Muldrew, D.B., Electrostatic resonances associated with the maximum frequencies of cyclotron-harmonic waves, *J. Geophys. Res.*, *77*, 1794-1801, 1972b.

Muldrew, D.B., and E.L. Hagg, Properties of high-latitude ionospheric ducts deduced from Alouette II two-hop echoes, *Proc. IEEE*, *57*, 1128-1134, 1969.

Nelms, G.L., and G.E.K. Lockwood, Early results from the topside sounder in the Alouette II satellite, in *Space Research VII*, edited by R.L. Smith-Rose, pp. 604-623, North-Holland Publishing Co., Amsterdam, 1967.

Nsumei, P.A., X. Huang, B.W. Reinisch, P. Song, V.M. Vasyliunas, J.L. Green, S.F. Fung, R.F. Benson, and D.L. Gallagher, Electron density over the northern polar region deduced from IMAGE/RPI sounding, *J. Geophys. Res.*, in press, 2002.

Osherovich, V.A., Physical nature of the diffuse plasma resonances in the ionosphere, *J. Geophys. Res.*, *92*, 316-320, 1987.

Osherovich, V.A., The physical nature of the upper subsidiary diffuse resonances, *J. Geophys. Res.*, *94*, 5530-5532, 1989.

Osherovich, V.A., and R.F. Benson, The lower subsidiary diffuse plasma resonances and the classification of radio emissions below the plasma frequency, *J. Geophys. Res.*, *96*, 19,331-19,341, 1991.

Osherovich, V.A., R.F. Benson, J. Fainberg, and B.W. Reinisch, Increased magnetospheric f_{pe}/f_{ce} values in response to magnetic-cloud enhancements of the solar-wind quasi-invariant on 31 March 2001, *Eos Trans. AGU*, *82 (47)*, Fall Meet. Suppl., Abstract SM31B-0758, 2001.

Osherovich, V.A., R.F. Benson, J. Fainberg, R.G. Stone, and R.J. MacDowall, Sounder stimulated Dn Resonances in Jupiter's Io plasma torus, *J. Geophys. Res.*, *98* (E10), 18751-18756, 1993.

Oya, H., Sequence of diffuse plasma resonances observed on Alouette 2 ionograms, *J. Geophys. Res.*, *75*, 4279-4285, 1970.

Oya, H., Verification of theory on weak turbulence relating to the sequence of diffuse plasma resonances in space, *Phys. Fluids*, *14*, 2487-2499, 1971.

Oya, H., Turbulence of electrostatic electron cyclotron harmonic waves observed by Ogo 5, *J. Geophys. Res.*, *77*, 3483-3494, 1972.

Oya, H., A. Morioka, K. Kobayashi, M. Iizima, T. Ono, H. Miyaoka, T. Okada, and T. Obara, Plasma wave observation and sounder experiments (PWS) using the Akebono (EXOS-D) satellite - Instrumentation and initial results including discovery of the high altitude equatorial plasma turbulence, *J. Geomagn. Geoelectr.*, *42*, 411-442, 1990.

Perraut, S., H.d. Feraudy, A. Roux, P.M.E. Decreau, J. Paris, and L. Matson, Density measurements in key regions of the Earth's magnetosphere: Cusp and auroral region, *J. Geophys. Res.*, *95*, 5997-6014, 1990.

Reinisch, B.W., D.M. Haines, K. Bibl, G. Cheney, I.A. Gulkin, X. Huang, S.H. Myers, G.S. Sales, R.F. Benson, S.F. Fung, J.L. Green, W.W.L. Taylor, J.-L. Bougeret, R. Manning, N. Meyer-Vernet, M. Moncuquet, D.L. Carpenter, D.L. Gallagher, and P. Reiff, The radio plasma imager investigation on the IMAGE spacecraft, *Space Sci. Rev.*, *91* (2), 319-359, 2000.

Reinisch, B.W., X. Huang, D.M. Haines, I.A. Galkin, J.L. Green, R.F. Benson, S.F. Fung, W.W.L. Taylor, P.H. Reiff, D.L. Gallagher, J.-L. Bougeret, R. Manning, D.L. Carpenter, and S.A. Boardsen, First results from the radio plasma imager on IMAGE, *Geophys. Res. Lett.*, *28*, 1167-1170, 2001a.

Reinisch, B.W., X. Huang, P. Song, G.S. Sales, S.F. Fung, J.L. Green, D.L. Gallagher, and V.M. Vasyliunas, Plasma density distribution along the magnetospheric field: RPI observations from IMAGE, *Geophys. Res. Lett.*, *28*, 4521-4524, 2001b.

Stix, T.H., The Theory of Plasma Waves, 283 pp., McGraw-Hill, New York, 1962.

Trotignon, J.G., P.M.E. Decreau, J.L. Rauch, and et al., How to determine the thermal electron density and the magnetic field strength from the Cluster/Whisper observations around the earth, *Ann. Geophysicae*, *19*, 1711-1720, 2001.

Trotignon, J.G., J. Etcheto, and J.P. Thouvenin, Automatic determination of the electron density measured by the relaxation sounder on board ISEE 1, *J. Geophys. Res.*, *91* (A4), 4302-4320, 1986.

Tsyganenko, N.A., Modeling the Earth's magnetospheric magnetic field confined within a realistic magnetopause, *J. Geophys. Res.*, *100* (A4), 5599-5612, 1995.

Tsyganenko, N.A., Effects of the solar wind conditions on the global magnetospheric configuration as deduced from data-based field models, in *3rd International Conference on Substorms (ICS-3)*, pp. 181-185, ESA SP-389, Versailles, France, 1996.

Tsyganenko, N.A., and D.P. Stern, Modeling the global magnetic field of the large-scale Birkeland current systems, *J. Geophys. Res.*, *101*, 27,187-27,198, 1996.

Warnock, J.M., Sideband structure observed by topside sounders, *Proc. IEEE*, *57*, 1135-1139, 1969.

Warren, E.S., and E.L. Hagg, Observation of electrostatic resonances of the ionospheric plasma, *Nature*, *220*, 466-468, 1968.

[1]Goddard Space Flight Center, Greenbelt, MD 20771, 301-286-4037, u2rfb@lepvax.gsfc.nasa.gov; V A Osherovich, L-3 Analytics/Goddard Space Flight Center, Greenbelt, MD 20771, 301-286-3649; J Fainberg, Goddard Space Flight Center, Greenbelt, MD 20771, 301-286-6940; B W Reinisch, University of Massachusetts Lowell, Lowell, MA 01854, 978-934-4903

Figure Captions

Figure 1. Normalized (by f_{ce}) frequencies as a function of f_{pe}/f_{ce} corresponding to (i) Qn frequencies (red curves), calculated from the es dispersion equation rather than the approximation (4) (see the discussion pertaining to Figure 4 of *Benson et al*. [2001b]), (ii) Dn^+, Dn and Dn^- frequencies (upper, middle and lower green curves in each band, respectively) from (7) – (9) truncated at the bounding nf_{ce} and f_{pe} values, (iii) f_{pe} (black line at 45°), and (iv) f_{uh} {from (3)}, f_x {from (5)} and f_z {from (6)} (blue curves).

Figure 2. A portion of an RPI plasmagram recorded on the X antenna at 0306:07 UT on 11 August 2000 using program 36 (3-79 kHz in 127 0.6 kHz steps, using two 3.2 ms pulses/frequency, in 63 s). The echo virtual range, expressed in earth radii (R_E = 6371 km), is displayed from 0-2.2 R_E (corresponding to delay times out to 93 ms) as a function of sounder frequency from 15-75 kHz. The color-coded echo amplitude scale has been selected to range from 40-63 dBnV/m (dB relative to 1nV/m input signal), using the capabilities of the analysis program known as BinBrowser [*Galkin et al.*, 2001], in order to highlight the resonances and X-mode reflection trace. An "X" at the top of the figure identifies the cutoff for this trace. The subscripts for the frequency designations of the other resonances are also identified at the top of the figure. The nf_{ce} resonances with n = 2 & 3 are identified by their n values. The diagram on the right side illustrates the location of IMAGE at the start of the plasmagram (4.2 R_E, 13.5 magnetic local time (MLT), 81.0 invariant latitude (INLAT)) as a red dot along it's orbit in relation to the projection of the model L = 4 field lines on the orbit plane.

Figure 3. An RPI plasmagram recorded on the X antenna during an outbound plasmapause crossing at 2209:19 UT on 5 December 2000 using program 39 (150-195 kHz in 151 0.3 kHz steps, sampling virtual range to 4.2 R_E (corresponding to delay times to 178 ms) after each 3.2 ms pulse, in 41 s). The measure values for f_z, f_{pe}, f_{uh}, f_{Q3}, f_x and $4f_{ce}$ are 153.6 ± 0.1, 169.9 ± 0.1, 174.6 ± 0.1, 182.4 ± 0.1, 190.2 ± 0.3 and 194.1 ± 0.1 kHz, respectively. The subscripts for the frequency designations of these features are identified at the top of the figure except for $4f_{ce}$ which is identified by the numeral 4. The echo amplitude scale has been selected to range from 9-59 dBnV/m. IMAGE location: 2.9 R_E, 7.5 MLT, 60.7 INLAT.

Figure 4. (a) N_e values deduced from passive RPI dynamic spectral peaks (assuming they occur at f_{pe}) as red filled circles, and from active soundings based on RPI programs # 35 (7% frequency step interval) as blue filled triangles and # 39 (300 Hz frequency step interval) as open green circles. The latter correspond to the resonances and cutoffs of Figure 3. The error bars associated with the dynamic spectral peaks are based on the 2% frequency step intervals used in RPI program #26 and a 5% f_{pe} identification uncertainty (see text). Straight dashed lines connect individual measurements. The blue error bars associated with RPI program # 35 are based on f_x + 3% and - 7% because of the uncertainty in projecting the reflection trace to zero virtual range. See the text for a discussion of Δpp. (b) An enlarged view of the region containing the N_e values deduced

from the resonances and cutoffs of Figure 3. Straight dashed lines connect individual measurements believed to contain the most reliable estimates of N_e.

Figure 5. Portions of RPI plasmagrams recorded on the Z antenna at (a) 0202:57 UT on 30 March 2001 (prior to magnetic storm) and (b) 1611:03 UT on 31 March 2001 (during a magnetic storm) using program 38 (3-48 kHz in 151 0.3 kHz steps, sampling the virtual range to 4.2 R_E after each 3.2 ms pulse, in 49 s). In each case, the swept-frequency range from 6-48 kHz is presented using an echo amplitude scale from 40-68 dBnV/m (the frequency region below 6 kHz does not produce useful sounding observations for plasma resonances). The measured values for f_{ce}, f_{D1}, f_{D1+}, $2f_{ce}$, f_{pe}, f_{uh}, f_{Q2}, $3f_{ce}$, f_{Q3}, $4f_{ce}$, f_{Q4}, $5f_{ce}$, f_{Q5}, $6f_{ce}$ and f_{Q6} are 8.0, 11.1, 13.5, 15.9, 18.0, 19.5, 20.2, 23.9, 25.4, 31.8, 32.5, 39.3, 39.7, 47.4 and 47.7 kHz, respectively, where the uncertainty on most values is estimated to be ± 0.1 kHz. The subscripts for the frequency designations of these features are identified at the top of the figure except for the nf_{ce} resonances which are identified by the appropriate n value. IMAGE location: 8.0 R_E, 11.0 MLT, 82.0 INLAT in (a) and 6.8 R_E, 24.0 MLT, 80.8 INLAT in (b).

Figure 6. Three-antenna normalized (by f_{ce} =7.96 kHz) representation of the mean of the signal amplitudes in the first 10 range bins (red) and in all of the range bins (black) for the data corresponding to the time interval of Figure 5b. The vertical green lines identified in the top frame correspond to calculated values based on the input f_{pe} (= 18.0 kHz) and f_{ce} values.

Figure 7. Three-antenna representation of the data corresponding to the time interval of Figure 5b using a plasmagram format where the signal-amplitudes are displayed as color-coded contours as a function of range bin vs. frequency normalized by f_{ce} = 7.96 kHz. Each range bin corresponds to 3.2 ms of delay time or 480 km = 7.53×10^{-2} R_E of virtual range. The longer tick marks correspond to the scaled input values for nf_{ce} and f_{pe} (= 18.0 kHz). The shorter tick marks correspond to the indicated calculated values based on these input values. Two of the shorter tick marks, corresponding to calculated resonances that overlap other principle resonances, are not labeled (D2+ near $2f_{ce}$ and D2 near f_{pe}).

Figure 8. Magnetospheric RPI resonant values superimposed on a composite normalized presentation (adapted from *Oya* [1971], *Benson* [1982] and *Osherovich, and Benson* [1991]) of Alouette-2 and ISIS-1 ionospheric topside-sounder resonances. The RPI values from Figures 2, 3 and 5b are shown as red dots at f_{pe}/f_{ce} = 0.98, 3.40 and 2.26, respectively.

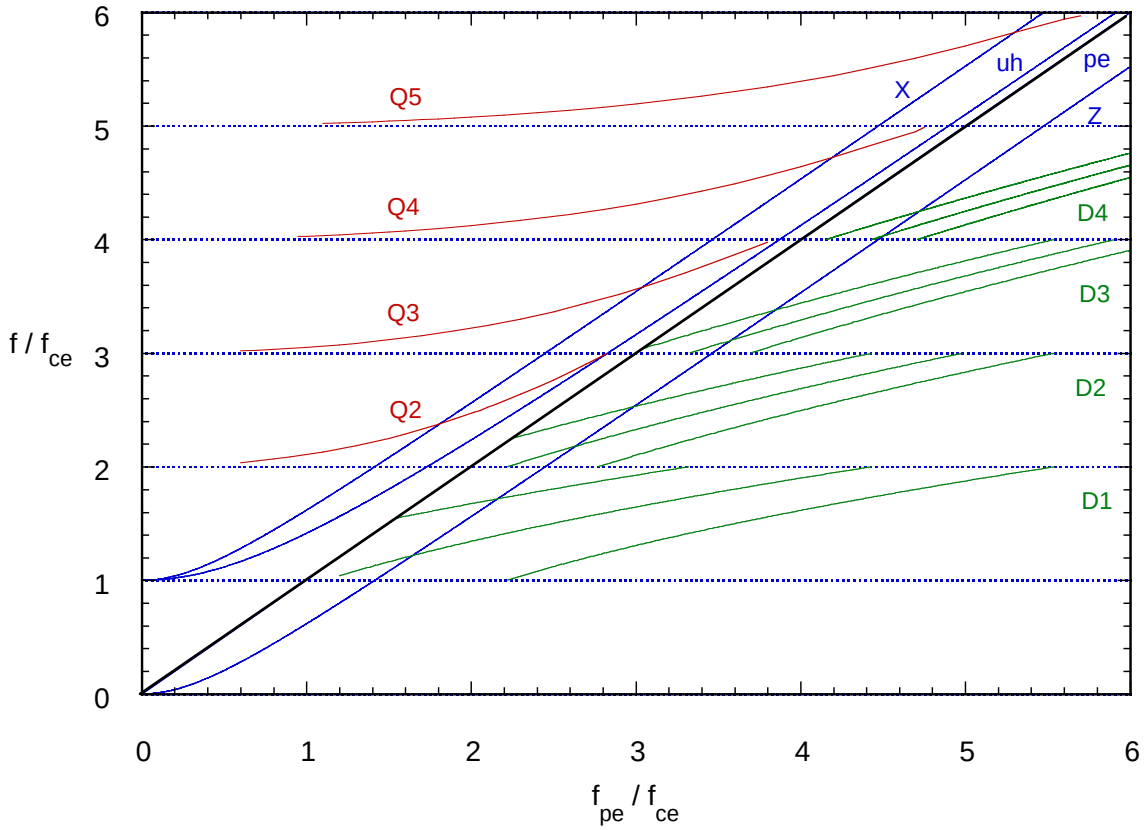

Figure 1. Normalized (by f_{ce}) frequencies as a function of f_{pe}/f_{ce} corresponding to (i) Qn frequencies (red curves), calculated from the es dispersion equation rather than the approximation (4) (see the discussion pertaining to Figure 4 of *Benson et al*. [2001b]), (ii) Dn^+, Dn and Dn^- frequencies (upper, middle and lower green curves in each band, respectively) from (7) – (9) truncated at the bounding nf_{ce} and f_{pe} values, (iii) f_{pe} (black line at 45°), and (iv) f_{uh} {from (3)}, f_x {from (5)} and f_z {from (6)} (blue curves).

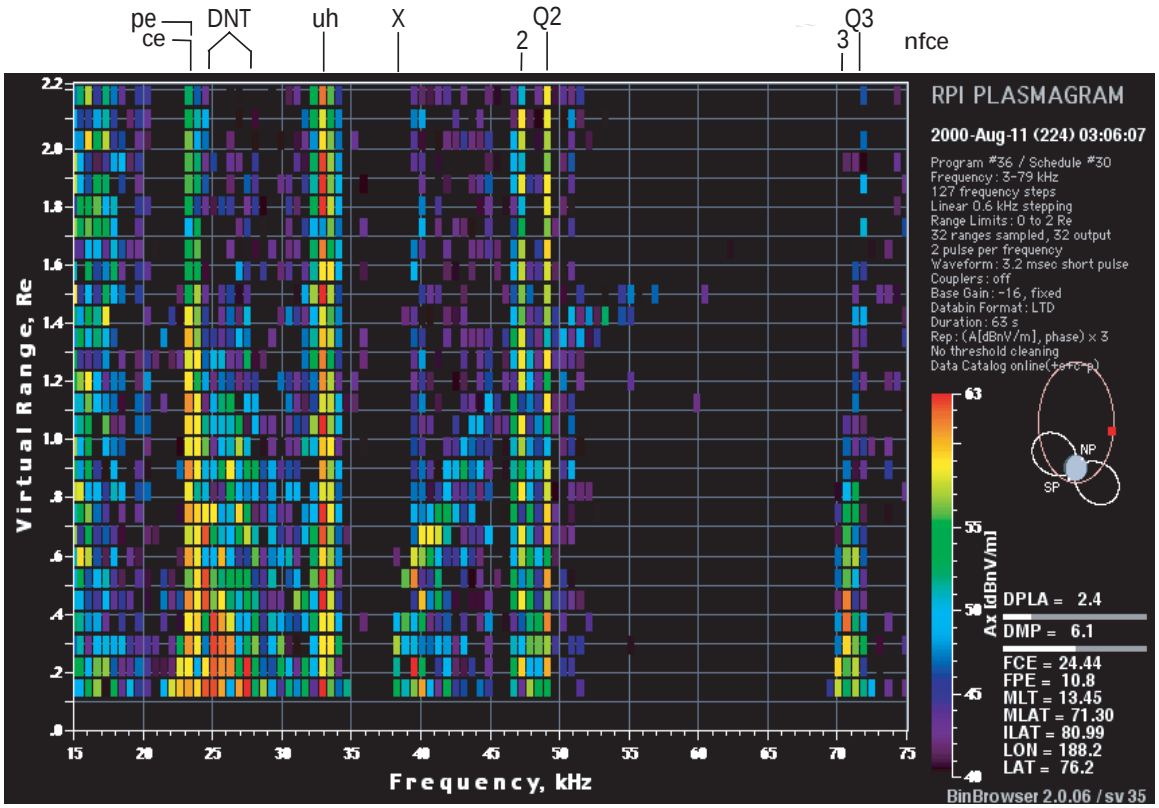

Figure 2. A portion of an RPI plasmagram recorded on the X antenna at 0306:07 UT on 11 August 2000 using program 36 (3-79 kHz in 127 0.6 kHz steps, using two 3.2 ms pulses/frequency, in 63 s). The echo virtual range, expressed in earth radii (R_E = 6371 km), is displayed from 0-2.2 R_E (corresponding to delay times out to 93 ms) as a function of sounder frequency from 15-75 kHz. The color-coded echo amplitude scale has been selected to range from 40-63 dBnV/m (dB relative to 1nV/m input signal), using the capabilities of the analysis program known as BinBrowser [*Galkin et al.*, 2001], in order to highlight the resonances and X-mode reflection trace. An "X" at the top of the figure identifies the cutoff for this trace. The subscripts for the frequency designations of the other resonances are also identified at the top of the figure. The nf_{ce} resonances with n = 2 & 3 are identified by their n values. The diagram on the right side illustrates the location of IMAGE at the start of the plasmagram (4.2 R_E, 13.5 magnetic local time (MLT), 81.0 invariant latitude (INLAT)) as a red dot along it's orbit in relation to the projection of the model L = 4 field lines on the orbit plane.

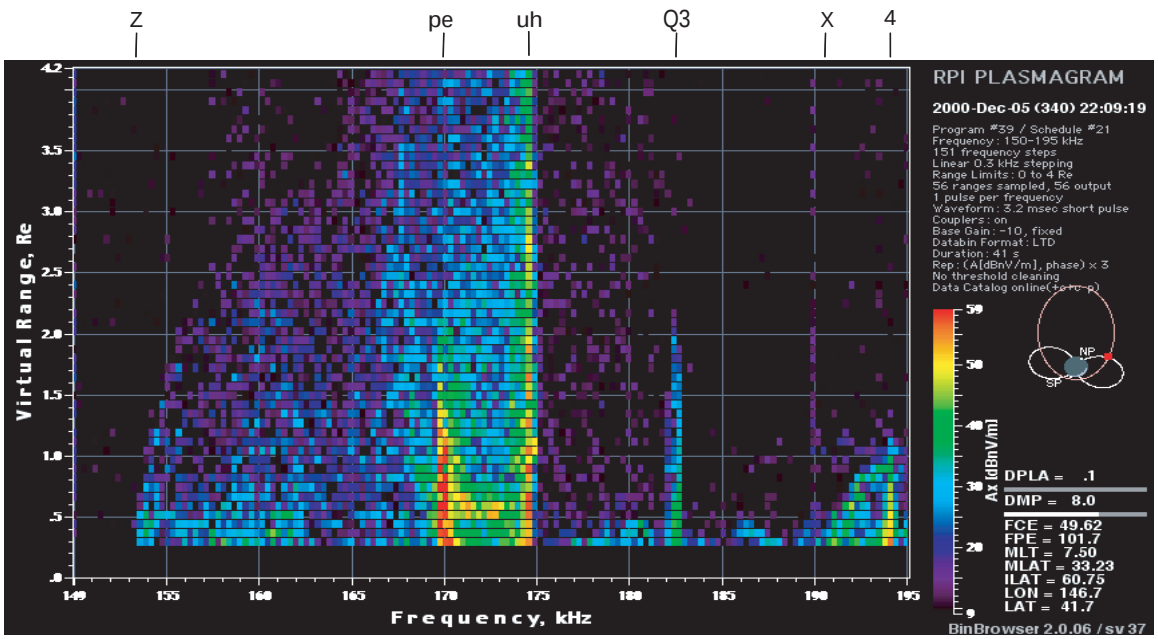

Figure 3. An RPI plasmagram recorded on the X antenna during an outbound plasmapause crossing at 2209:19 UT on 5 December 2000 using program 39 (150-195 kHz in 151 0.3 kHz steps, sampling virtual range to 4.2 R_E (corresponding to delay times to 178 ms) after each 3.2 ms pulse, in 41 s). The measure values for f_z, f_{pe}, f_{uh}, f_{Q3}, f_x and $4f_{ce}$ are 153.6 ± 0.1, 169.9 ± 0.1, 174.6 ± 0.1, 182.4 ± 0.1, 190.2 ± 0.3 and 194.1 ± 0.1 kHz, respectively. The subscripts for the frequency designations of these features are identified at the top of the figure except for $4f_{ce}$ which is identified by the numeral 4. The echo amplitude scale has been selected to range from 9-59 dBnV/m. IMAGE location: 2.9 R_E, 7.5 MLT, 60.7 INLAT.

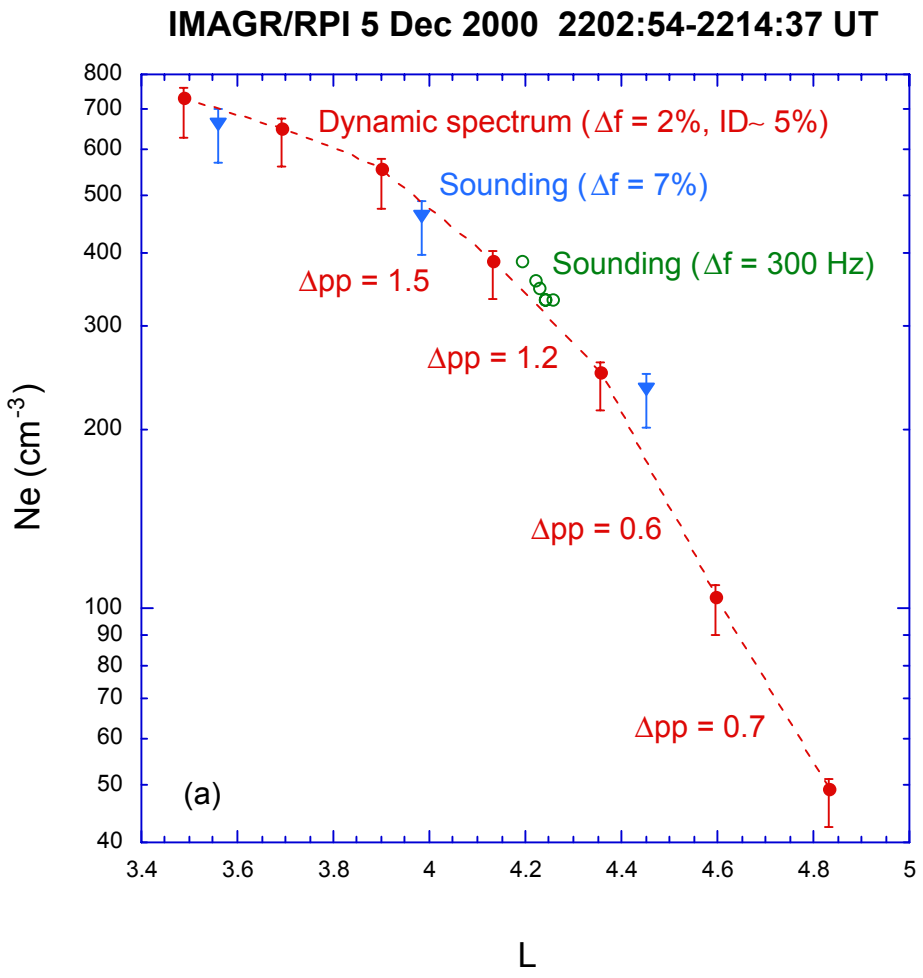

Figure 4. (a) N_e values deduced from passive RPI dynamic spectral peaks (assuming they occur at f_{pe}) as red filled circles, and from active soundings based on RPI programs # 35 (7% frequency step interval) as blue filled triangles and # 39 (300 Hz frequency step interval) as open green circles. The latter correspond to the resonances and cutoffs of Figure 3. The error bars associated with the dynamic spectral peaks are based on the 2% frequency step intervals used in RPI program #26 and a 5% f_{pe} identification uncertainty (see text). Straight dashed lines connect individual measurements. The blue error bars associated with RPI program # 35 are based on f_x + 3% and - 7% because of the uncertainty in projecting the reflection trace to zero virtual range. See the text for a discussion of Δpp.

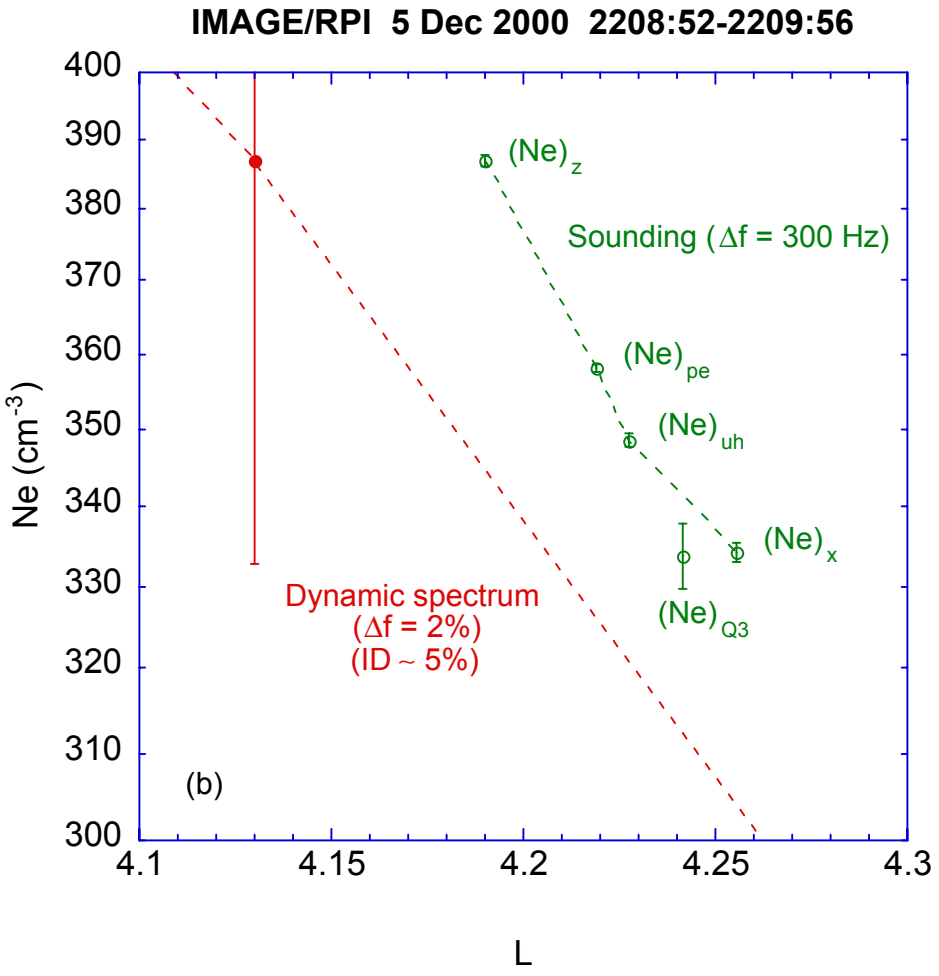

Figure 4. (b) An enlarged view of the region containing the N_e values deduced from the resonances and cutoffs of Figure 3. Straight dashed lines connect individual measurements believed to contain the most reliable estimates of N_e.

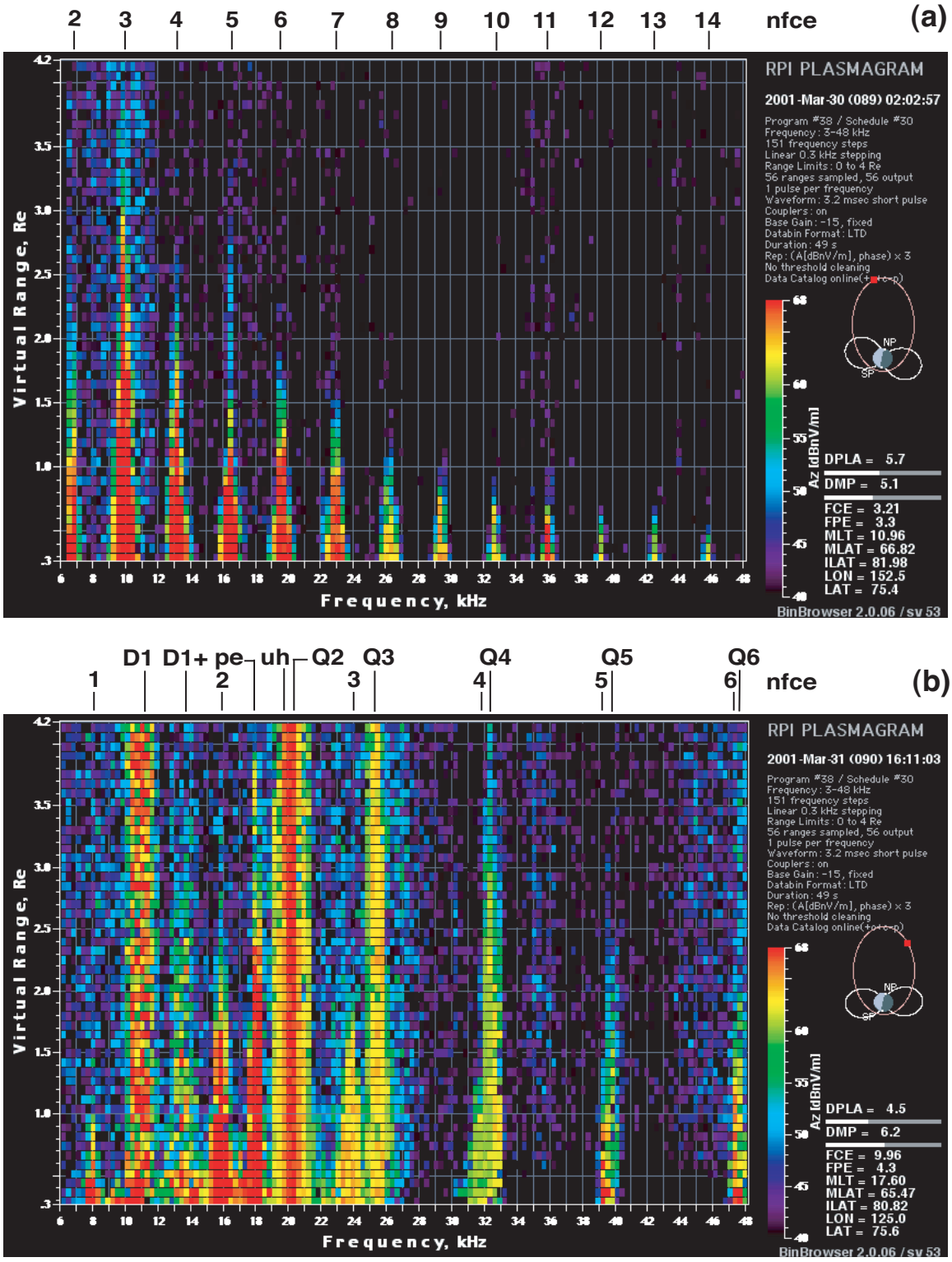
2 3 4 5 6 7 8 9 10 11 12 13 14 nfce
(a)
RPI PLASMAGRAM
2001-Mar-30 (089) 02:02:57
Program #38 / Schedule #30
Frequency: 3-48 kHz
151 frequency steps
Linear 0.3 kHz stepping
Range Limits: 0 to 4 Re
56 ranges sampled, 56 output
1 pulse per frequency
Waveform: 3.2 msec short pulse
Couplers: on
Base Gain: -15, fixed
Databin Format: LTD
Duration: 49 s
Rep: (A[dBnV/m], phase) x 3
No threshold cleaning
Data Catalog online(+o+c-p)
NP
SP
Az [dBnV/m]
DPLA = 5.7
DMP = 5.1
FCE = 3.21
FPE = 3.3
MLT = 10.96
MLAT = 66.82
ILAT = 81.98
LON = 152.5
LAT = 75.4
BinBrowser 2.0.06 / sv 53
Virtual Range, Re
Frequency, kHz
1 D1 D1+ 2 pe uh Q2 3 Q3 4 Q4 5 Q5 6 Q6 nfce
(b)
RPI PLASMAGRAM
2001-Mar-31 (090) 16:11:03
Program #38 / Schedule #30
Frequency: 3-48 kHz
151 frequency steps
Linear 0.3 kHz stepping
Range Limits: 0 to 4 Re
56 ranges sampled, 56 output
1 pulse per frequency
Waveform: 3.2 msec short pulse
Couplers: on
Base Gain: -15, fixed
Databin Format: LTD
Duration: 49 s
Rep: (A[dBnV/m], phase) x 3
No threshold cleaning
Data Catalog online(+o+c-p)
NP
SP
Az [dBnV/m]
DPLA = 4.5
DMP = 6.2
FCE = 9.96
FPE = 4.3
MLT = 17.60
MLAT = 65.47
ILAT = 80.82
LON = 125.0
LAT = 75.6
BinBrowser 2.0.06 / sv 53
Virtual Range, Re
Frequency, kHz

Figure 5

Figure 5. Portions of RPI plasmagrams recorded on the Z antenna at (a) 0202:57 UT on 30 March 2001 (prior to magnetic storm) and (b) 1611:03 UT on 31 March 2001 (during a magnetic storm) using program 38 (3-48 kHz in 151 0.3 kHz steps, sampling the virtual range to 4.2 R_E after each 3.2 ms pulse, in 49 s). In each case, the swept-frequency range from 6-48 kHz is presented using an echo amplitude scale from 40-68 dBnV/m (the frequency region below 6 kHz does not produce useful sounding observations for plasma resonances). The measured values for f_{ce}, f_{D1}, f_{D1+}, $2f_{ce}$, f_{pe}, f_{uh}, f_{Q2}, $3f_{ce}$, f_{Q3}, $4f_{ce}$, f_{Q4}, $5f_{ce}$, f_{Q5}, $6f_{ce}$ and f_{Q6} are 8.0, 11.1, 13.5, 15.9, 18.0, 19.5, 20.2, 23.9, 25.4, 31.8, 32.5, 39.3, 39.7, 47.4 and 47.7 kHz, respectively, where the uncertainty on most values is estimated to be ± 0.1 kHz. The subscripts for the frequency designations of these features are identified at the top of the figure except for the nf_{ce} resonances which are identified by the appropriate n value. IMAGE location: 8.0 R_E, 11.0 MLT, 82.0 INLAT in (a) and 6.8 R_E, 24.0 MLT, 80.8 INLAT in (b).

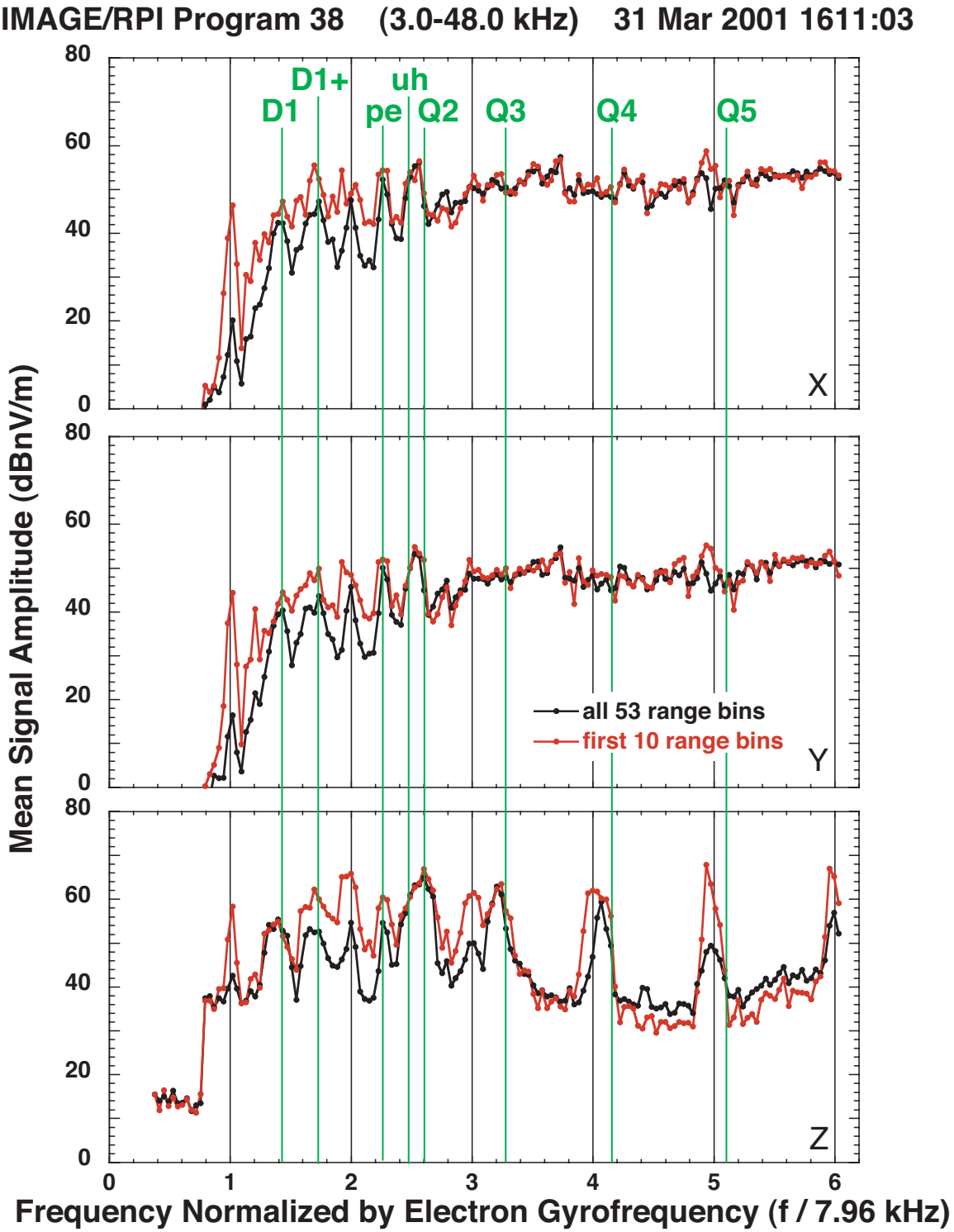
IMAGE/RPI Program 38 (3.0-48.0 kHz) 31 Mar 2001 1611:03
D1
D1+
uh
pe
Q2
Q3
Q4
Q5
X
Y
Z
all 53 range bins
first 10 range bins
Mean Signal Amplitude (dBnV/m)
Frequency Normalized by Electron Gyrofrequency (f / 7.96 kHz)

Figure 6

Figure 6. Three-antenna normalized (by f_{ce} =7.96 kHz) representation of the mean of the signal amplitudes in the first 10 range bins (red) and in all of the range bins (black) for the data corresponding to the time interval of Figure 5b. The vertical green lines identified in the top frame correspond to calculated values based on the input f_{pe} (= 18.0 kHz) and f_{ce} values.

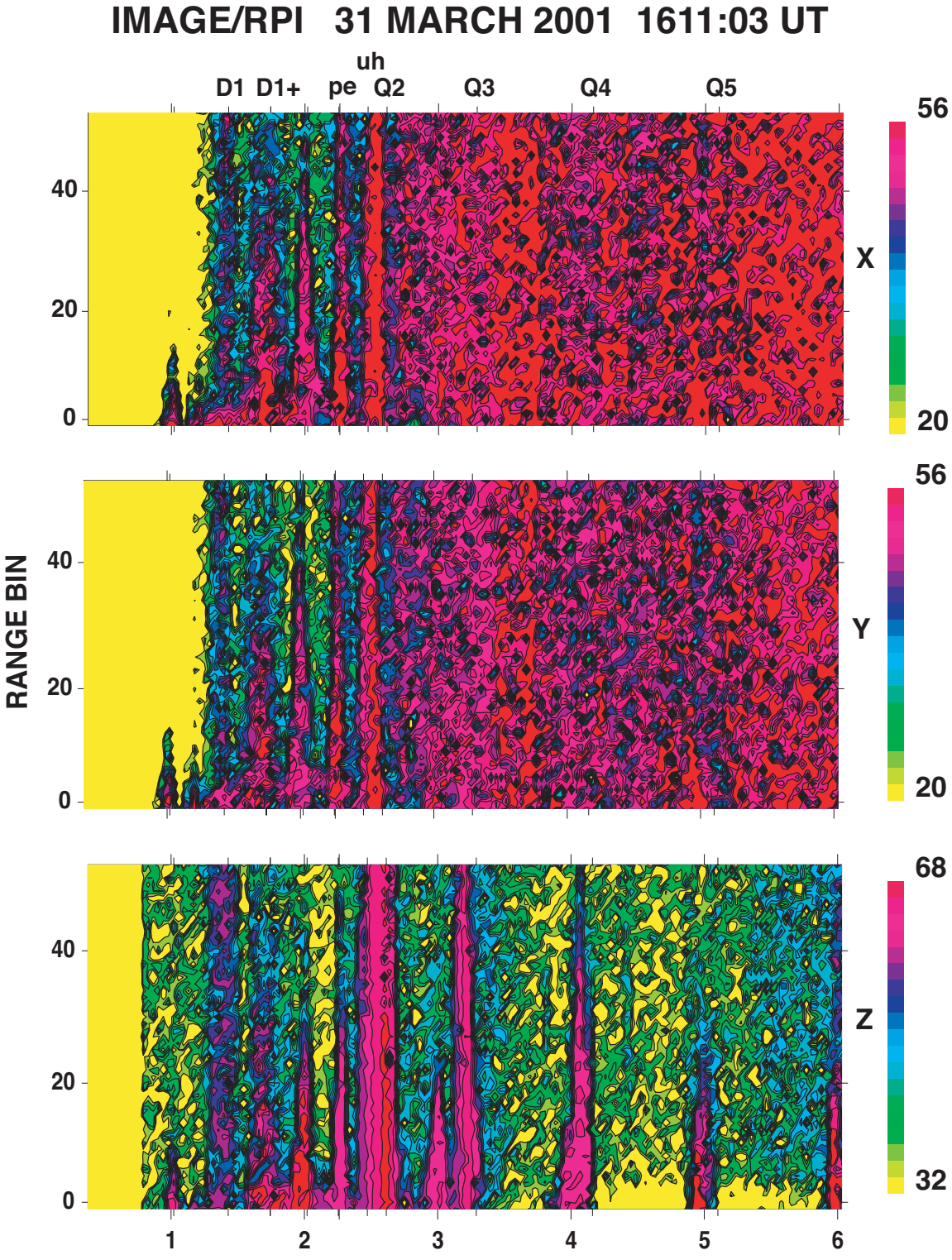
IMAGE/RPI 31 MARCH 2001 1611:03 UT
uh
D1 D1+ pe Q2 Q3 Q4 Q5
RANGE BIN
40
20
0
X
Y
Z
56
20
56
20
68
32
1
2
3
4
5
6
FREQUENCY NORMALIZED by fce = 7.96 kHz
(CALCULATIONS BASED on fpe = 18.0 kHz = 2.26 fce)

Figure 7

Figure 7. Three-antenna representation of the data corresponding to the time interval of Figure 5b using a plasmagram format where the signal-amplitudes are displayed as color-coded contours as a function of range bin vs. frequency normalized by f_{ce} = 7.96 kHz. Each range bin corresponds to 3.2 ms of delay time or 480 km = 7.53×10^{-2} R_E of virtual range. The longer tick marks correspond to the scaled input values for nf_{ce} and f_{pe} (= 18.0 kHz). The shorter tick marks correspond to the indicated calculated values based on these input values. Two of the shorter tick marks, corresponding to calculated resonances that overlap other principle resonances, are not labeled (D2+ near $2f_{ce}$ and D2 near f_{pe}).

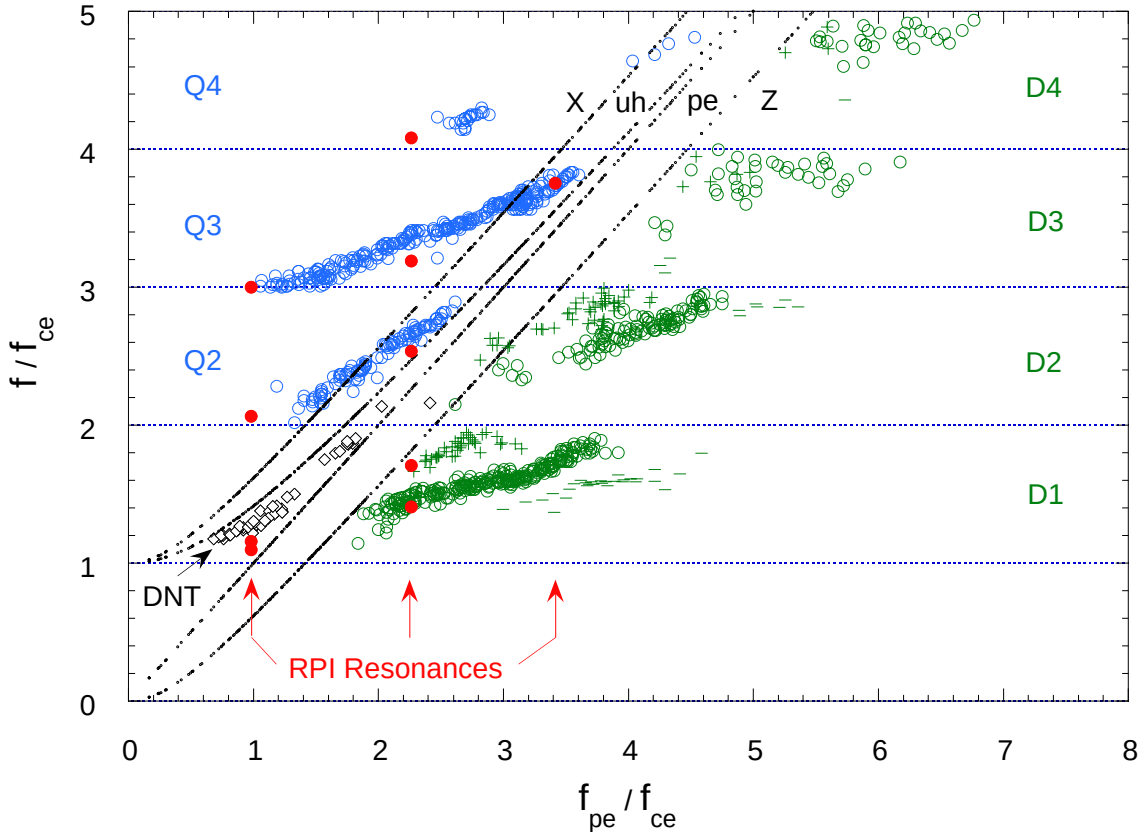

Figure 8. Magnetospheric RPI resonant values superimposed on a composite normalized presentation (adapted from *Oya* [1971], *Benson* [1982] and *Osherovich, and Benson* [1991]) of Alouette-2 and ISIS-1 ionospheric topside-sounder resonances. The RPI values from Figures 2, 3 and 5b are shown as red dots at f_{pe}/f_{ce} = 0.98, 3.40 and 2.26, respectively.